

A consistent and conservative volume distribution algorithm and its applications to multiphase flows using Phase-Field models

Ziyang Huang^{*1}, Guang Lin^{†1,2}, and Arezoo M. Ardekani^{‡1}

¹ *School of Mechanical Engineering, Purdue University, West Lafayette, IN 47907, USA*

² *Department of Mathematics, Purdue University, West Lafayette, IN 47907, USA*

(June 24, 2020)

Abstract

In the present study, the multiphase volume distribution problem, where there can be an arbitrary number of phases, is addressed using a consistent and conservative volume distribution algorithm. The proposed algorithm satisfies the summation constraint, the conservation constraint, and the consistency of reduction. The first application of the volume distribution algorithm is to develop a multiphase conservative Allen-Cahn model that satisfies the consistency of reduction. A corresponding consistent and conservative numerical scheme is developed for the model. The multiphase conservative Allen-Cahn model has a better ability than the multiphase Cahn-Hilliard model to preserve under-resolved structures. The second application is to develop a numerical procedure, called the boundedness mapping, to map the order parameters, obtained numerically from a multiphase model, into their physical interval, and at the same time to preserve the physical properties of the order parameters. Along with the consistent and conservative schemes for the multiphase Phase-Field models, the numerical solutions are consistent, conservative, and bounded, which have been carefully analyzed and numerically validated. Then, the multiphase Phase-Field models are coupled with the momentum equation by satisfying the consistencies of mass conservation and of mass and momentum transport, thanks to the consistent formulation. It is demonstrated that the proposed model and scheme converge to the sharp-interface solution and are capable of capturing the complicated multiphase dynamics even when there is a large density or viscosity ratio.

Keywords: *Multiphase flows; Volume distribution; Phase-Field models; Consistent scheme; Conservative scheme; Boundedness*

1 Introduction

Multiphase flows are ubiquitous and have wide-spread applications. Lots of efforts have been focused on modeling and simulating two-phase flows, and the one-fluid formulation [73, 58], where the motion of the fluids is governed by a single equation of their mixture, is one of the most popular ones. Under this framework, many successful numerical models or methods have been developed to specify locations of interfaces, e.g., the front-tracking method [74, 72], the level-set method [55, 69, 66, 23], the conservative level-set method [53, 54, 11], the volume-of-fluid (VOF) method [25, 63, 56], the THINC method [75, 31, 77, 59], and the Phase-Field (or Diffuse-Interface) method [2, 32, 67, 29]. A recent review of various interface-capturing methods is available in [50]. The surface tension can be modeled by the smoothed surface stress method [24], the continuous surface force (CSF) [6], the ghost fluid method (GFM) [18, 43], the conservative and well-balanced surface tension model [51], the Phase-Field method derived from the energy balance or the least-action principle [32, 79], and it is incorporated into the momentum equation by a balanced-force algorithm

^{*}Email: huan1020@purdue.edu

[†]Email: guanglin@purdue.edu; Corresponding author

[‡]Email: ardekani@purdue.edu; Corresponding author

[20]. A recent review of various numerical models for surface tension is available in [57]. The physical coupling between the mass and momentum transport is enforced numerically by a consistent scheme, e.g., [62, 8, 10, 56] for the volume-of-fluid (VOF) method, [60, 52] for the level-set method, [76] for the THINC method, and [29, 28] for the Phase-Field methods. Many recent studies investigate three-phase flows, e.g., [64, 65, 19, 46, 68, 4, 42, 37, 82, 81, 61], and even extend the model to general N -phase flows ($N \geq 1$), e.g., [5, 38, 39, 45, 40, 13, 14, 15, 16, 78]. Most of the three-phase models and all the N -phase models are implemented using a Phase-Field model due to its simplicity and effectiveness. In the Phase-Field model, a set of order parameters, which are commonly related to the volume fractions of the phases, are introduced to indicate the locations of different phases. The sharp interfaces are replaced by small but finite interfacial regions, inside which there are thermodynamical compression and diffusion of the model to preserve the thickness of the interfacial regions.

In the present work, we consider the multiphase volume distribution problem, where there can be an arbitrary number of phases. In some previous two-phase studies, this is also called the mass distribution or the mass redistribution. Since the problem is not related to the densities of individual phases, it is more precise to call it the volume distribution. Given the total volumes of individual phases to be distributed in the domain and a set of order parameters representing the locations of different phases, we need to specify the local volumes of individual phases to be distributed at every location of the domain. It should be noted that the domain is fixed. Therefore, before and after the volume distribution, the volume of the domain does not change. This is a kind of inverse problem and its solution is not necessarily unique. However, the admissible solution should satisfy the following physical properties. The first one is called the summation constraint, which requires that the summation of the order parameters is not changed by the volume distribution. It should be noted that the order parameters are not independent of each other and there is a summation constraint for the order parameters. For example, the summation of the order parameters has to be unity everywhere in the domain, if the order parameters are the volume fractions of the phases, and it should not be changed after the volume distribution. Otherwise, local void or overfilling is generated due to the volume distribution. The second one is called the conservation constraint, which requires the total added volumes of individual phases in the domain after the volume distribution to be equal to the corresponding given ones to be distributed. Otherwise, the volume distribution problem is not solved successfully. The last one is the consistency of reduction, which requires that the volume of a specific phase is not distributed to where that phase is absent. Otherwise, fictitious phases can be generated after the volume distribution. If the volume distribution satisfies all the aforementioned physical constraints, it is consistent and conservative. It is relatively straightforward to solve the volume distribution problem and to satisfy the physical constraints for two-phase cases, while it becomes non-trivial for general multiphase cases. In a two-phase case, increasing the volume of one of the two phases corresponds to a decrease of the same amount of volume of another phase, so that the summation constraint is satisfied. As a result, only one of the phases is necessarily considered and the volume distribution is phase-wise. In a general multiphase case, there can be more than two phases at a specific location. When any one of them changes its volume, the others have to respond to that simultaneously to satisfy the summation constraint. In other words, all the phases have to be considered at the same time. The interfacial regions always include the two phases considered in the two-phase case. However, the interfacial regions in the multiphase case can include more than two phases, and the phases included are varied from different interfacial regions. This also casts difficulty to satisfy the consistency of reduction in a general multiphase case. To the best of our knowledge, this problem has never been addressed in the previous studies.

The first application, motivated us to address the multiphase volume distribution problem, is to develop a multiphase conservative Allen-Cahn model that satisfies the consistency of reduction. Almost all the Phase-Field models for multiphase flows are Cahn-Hilliard type since it has a conservative form. Therefore, the mass conservation of each phase is satisfied. However, by adding a Lagrange multiplier, we can obtain the so-called conservative Allen-Cahn model, which satisfies the mass conservation as well. By appropriately designing the Lagrange multiplier, Brassel and Bretin [7] proposed a two-phase conservative Allen-Cahn model that is applicable for two-phase flow modeling. The two-phase conservative Allen-Cahn model is a 2nd-order partial differential equation, while the Cahn-Hilliard models are usually 4th order. Therefore the conservative Allen-Cahn model is easier to solve. In addition, it has a maximum principle so that its solution has an upper and lower bound. Both the analysis [7] and numerical comparison [44] suggest that the two-phase conservative Allen-Cahn model has a better ability than the Cahn-Hilliard models to preserve the

under-resolved structure. Our previous analysis [28] also shows that the two-phase conservative Allen-Cahn model satisfies the consistency of reduction. Therefore, it is attractive to develop a multiphase conservative Allen-Cahn model for multiphase flows. Such a model is developed by Kim and Lee [40]. Although they numerically show that their model is able to preserve small structures and their solution is inside the physical interval, the model violates the consistency of reduction. The consistency of reduction is of great importance for a multiphase model since it avoids generating fictitious phases. It has a significant effect on the flow dynamics, especially when the density ratio or viscosity ratio in the problem is large. For example, in a water-oil-air system, the maximum density and viscosity ratios are on the order of 1000. Violating the consistency of reduction can unphysically generate the oil at the interface of a water-air bubble. The bubble becomes much heavier and more viscous than it should be even though only a small amount of the oil is generated. Therefore, the rising motion of the bubble is slowed down due to violating the consistency of reduction. This behavior has been demonstrated in [5]. With the help of the consistent and conservative volume distribution algorithm, a multiphase conservative Allen-Cahn model is developed in this work, which satisfies the consistency of reduction. To the best of our knowledge, this is the first multiphase conservative Allen-Cahn model that is reduction consistent. A corresponding consistent and conservative scheme is developed, which preserves all the physical properties of the model at the discrete level.

The second application related to the multiphase volume distribution problem is to map the order parameters into their physical interval. In the multiphase flows, the order parameters are not only the indicator of different phases but are also used to compute the density and viscosity of the fluid mixture. This computation is based on the assumption that the order parameters have a physical bound. For example, the order parameters should be in $[0, 1]$ if they are the volume fractions. If some of the order parameters are beyond their physical interval, the density of the fluid mixture, for example, can be smaller than the minimum density of the phases, and can even be negative, resulting in an ill-posed momentum equation. A problem is less tolerant to the out-of-bound order parameters when it has a large density or viscosity ratio. The out-of-bound order parameters can be generated due to the defect of the model. For example, the widely-used two-phase Cahn-Hilliard model [67], with constant mobility and the Ginzburg-Landau double-well potential, admits an out-of-bound solution [80, 70, 9, 21]. Fortunately, both the asymptotic analysis [47, 1], and the scaling analysis [80] suggest that the out-of-bound issue is controlled by the interface thickness, which is normally as small as the grid size. Another source of the out-of-bound order parameters is from numerical errors, even though the model has the maximum principle. However, designing a bound-preserving scheme is not a trivial task, especially when the model is non-linear and complicated. In addition, the bound-preserving scheme usually casts an additional constraint on the time step, e.g., [49] for the two-phase conservative Phase-Field model [12], and [28] for the two-phase conservative Allen-Cahn model [7]. The out-of-bound issue from the numerical error is the truncation error of the scheme, which again is related to the grid size. Since the out-of-bound error from either the defect of the model or the numerical error is related to the grid size, which is usually small, a more common practice is to clip the out-of-bound solution, e.g., in [12, 17, 16]. However, a volume distribution algorithm has to be supplemented following the clipping operation. Otherwise, the mass conservation is destroyed [26]. Chiu and Lin [12] evenly distributed the volume, which is lost from the clipping operation, to the interfacial regions, and this algorithm is applied in [83]. Huang et al. [28] distributed the volume based on a weight function that is the same as the one in the two-phase conservative Allen-Cahn model [7]. The clipping operation is also commonly used in the volume-of-fluid (VOF) or THINC methods, e.g., [3, 22, 59], and a volume distribution algorithm is required to achieve mass conservation [3]. As discussed, the multiphase volume distribution problem is far more challenging than the two-phase one and, thus, both the clipping operation and the volume distribution have to be carefully designed. Otherwise, the physical properties of the order parameters can be violated, i.e., the summation of the order parameters is changed or fictitious phases are generated after those operations. To the best of our knowledge, this solution has never been proposed in previous studies. Thanks to the consistent and conservative volume distribution algorithm, we develop a numerical procedure for multiphase problems, called the boundedness mapping, which maps the order parameters, obtained numerically from a multiphase model, into their physical interval, and at the same time, the physical properties of the order parameters, i.e., their summation constraint, mass conservation, and consistency of reduction, are preserved.

To simulate multiphase flows, the Phase-Field models need to be coupled with the momentum equation appropriately by satisfying the consistency of mass conservation and the consistency of mass and momentum transport. Otherwise, unphysical velocity fluctuations and interface deformation appear, and can result

in numerical instability, especially in problems with large density ratios, which have been analyzed and demonstrated in our previous studies for two- and multi-phase flows [29, 27, 28]. This casts another challenge. In the multiphase conservative Allen-Cahn model, there is a Lagrangian multiplier to enforce the mass conservation. Therefore, the conservative Allen-Cahn model is not in a conservative form and the consistency analysis proposed in [29] is not valid. Although the multiphase Cahn-Hilliard model is in a conservative form, the boundedness mapping modified its out-of-bound solution, which contributes to the violation of the consistency conditions. Actually, this issue was neither addressed nor discussed in many previous studies for two-phase flows using the volume-of-fluid (VOF) or Phase-Field methods, where the clipping and volume distribution were performed, although the schemes in those studies were claimed to be consistent. We addressed this issue in [28], where the two-phase conservative Allen-Cahn model is applied to study two-phase flows. The consistent formulation is proposed to deal with the Lagrange multiplier in the Phase-Field model so that the consistencies of reduction, mass conservation, and mass and momentum transport are satisfied. In addition, the boundedness mapping can be represented as a Lagrange multiplier in the models and it is treated in the same manner. In the present study, the consistent formulation is applied to the multiphase case to enforce the consistency conditions. Combining the scheme for the multiphase Cahn-Hilliard model in our previous work [27] or the scheme for the multiphase conservative Allen-Cahn model in the present work and the boundedness mapping with the consistent formulation [28] and the scheme for the momentum equation [29, 27], we can show that the overall scheme satisfies the mass conservation of each phase, the momentum conservation without interfacial tensions, the summation constraint for the order parameters, the boundedness of the order parameters, and the consistencies of reduction, of mass conservation, and mass and momentum transport. The momentum conservation including the interfacial tensions is achievable by appropriately choosing the method for the surface force, see [27]. We demonstrate that the proposed model and scheme are capable of capturing the complicated multiphase dynamics even when there is a large density or viscosity ratio.

The rest of the paper is organized as follows. In Section 2, the multiphase problem is defined, followed by the introduction of the governing equations and the application of the consistent formulation. Then, the numerical schemes for the governing equations are summarized. In Section 3, the consistent and conservative volume distribution algorithm is elaborated, followed by its applications to develop the multiphase conservative Allen-Cahn model that satisfies the consistency of reduction and to develop the boundedness mapping to map the order parameters into their physical interval. In Section 4, various numerical tests are performed to validate the properties of the models and their schemes and to demonstrate their capability in solving complicated multiphase flows. In Section 5, the present study is concluded.

2 Governing equations and discretizations

In this section, the problem of interest is first defined, after which the governing equations are introduced. At the end of this section, we briefly summarize the numerical schemes for the governing equations.

2.1 Problem definition

In the present work, we confine our study to multiphase incompressible flows where the number of phases is N ($N \geq 1$). All the phases are immiscible with each other and have their own constant densities $\{\rho_p\}_{p=1}^N$ and viscosities $\{\mu_p\}_{p=1}^N$. Each pair of phases has a surface tension $\sigma_{p,q}$. The locations of the phases are represented by a set of order parameters $\{\phi_p\}_{p=1}^N$, which specifically is the volume fraction contrasts. The physical range of $\{\phi_p\}_{p=1}^N$ is in $[-1, 1]$. Therefore, the bulk-phase region of phase p is where $\phi_p = 1$, while phase p is absent where $\phi_p = -1$. The order parameters are not independent and their summation should satisfy the summation constraint for the order parameters, i.e.,

$$\sum_{p=1}^N \phi_p = 2 - N. \quad (1)$$

Eq.(1) is equivalent to the summation of the volume fractions of the phases being unity if the volume fractions $\{C_p\}_{p=1}^N$ is defined as

$$C_p = \frac{1 + \phi_p}{2}, \quad 1 \leq p \leq N. \quad (2)$$

Without considering any sources of the phases in or at the boundary of the domain, the mass conservation of individual phases require that

$$\frac{d}{dt} \int_{\Omega} \phi_p d\Omega = 0, \quad 1 \leq p \leq N. \quad (3)$$

The density and viscosity of the fluid mixture are

$$\rho = \sum_{p=1}^N \rho_p C_p = \sum_{p=1}^N \rho_p \frac{1 + \phi_p}{2}, \quad (4)$$

$$\mu = \sum_{p=1}^N \mu_p C_p = \sum_{p=1}^N \mu_p \frac{1 + \phi_p}{2}. \quad (5)$$

The flow is incompressible so its velocity \mathbf{u} is divergence-free, i.e.,

$$\nabla \cdot \mathbf{u} = 0 \quad (6)$$

2.2 Governing equations

As discussed in our previous work [27], the following three consistency conditions are of great importance for a multiphase flow model. The definitions of the consistency conditions are

- the consistency of reduction: An N -phase system should be able to recover the corresponding M -phase system ($1 \leq M \leq N - 1$) when $(N - M)$ phases are absent.
- the consistency of mass conservation: The mass conservation equation should be consistent with the transport equation defined from the Phase-Field equation and the density of the fluid mixture. The mass flux in the mass conservation equation should lead to a zero mass source.
- the consistency of mass and momentum transport: The momentum flux in the momentum equation should be a tensor product between the mass flux and the flow velocity, where the mass flux should be identical to the one in the mass conservation equation.

The consistency of reduction guarantees that fictitious phases are not allowed to be generated by the model and the model is able to recover the sing-phase dynamics inside individual bulk-phase regions. The consistency of mass conservation and the consistency of mass and momentum transport ensures the compatibility between the mass and momentum equations.

2.2.1 Multiphase Phase-Field models

The order parameters are governed by a multiphase Phase-Field model, and the Phase-Field model is either the Cahn-Hilliard type or the conservative Allen-Cahn type. In the present work, we consider the Phase-Field model to be the Cahn-Hilliard type if a Phase-Field model is written in a conservative form. On the other hand, if a Phase-Field model includes Lagrange multipliers to enforce the mass conservation, i.e., Eq.(3), it belongs to the conservative Allen-Cahn type. A physically admissible Phase-Field model not only ensures the summation constraint Eq.(1) and the mass conservation Eq.(3) but also the consistency of reduction.

Specifically, we consider the multiphase Phase-Field model in [16, 27] as the representative of the Cahn-Hilliard type model, and the Phase-Field equation reads

$$\frac{\partial \phi_p}{\partial t} + \nabla \cdot (\mathbf{u} \phi_p) = \nabla \cdot \left(\sum_{q=1}^N M_{p,q} \nabla \xi_q \right), \quad 1 \leq p \leq N, \quad (7)$$

where

$$M_{p,q} = \begin{cases} -M_0(1 + \phi_p)(1 + \phi_q), p \neq q, \\ M_0(1 + \phi_p)(1 - \phi_q), p = q, \end{cases} \quad (8)$$

is the mobility between phases p and q ,

$$\xi_p = \sum_{q=1}^N \lambda_{p,q} \left(\frac{1}{\eta^2} (g'_1(\phi_p) - g'_2(\phi_p + \phi_q)) + \nabla^2 \phi_q \right), \quad (9)$$

is the chemical potential of phase p . M_0 is a positive constant. $g_1(\phi) = \frac{1}{4}(1 - \phi^2)^2$ and $g_2(\phi) = \frac{1}{4}\phi^2(\phi + 2)^2$ are the potential functions, and $g'_1(\phi)$ and $g'_2(\phi)$ are their derivatives with respect to ϕ . $\lambda_{p,q} = \frac{3}{2\sqrt{2}}\sigma_{p,q}\eta$ is the mixing energy density of phases p and q , where η is the thickness of the interface. The Cahn-Hilliard model Eq.(7) honors the summation constraint Eq.(1), the mass conservation Eq.(3), and the consistency of reduction.

The multiphase conservative Allen-Cahn model considered in the present work reads

$$\frac{\partial \phi_p}{\partial t} + \nabla \cdot (\mathbf{u} \phi_p) = M_0 \lambda_0 \nabla^2 \phi_p - \frac{M_0 \lambda_0}{\eta^2} \left(g'_1(\phi_p) - \frac{1 + \phi_p}{2} L^s \right) + L_p^c, \quad 1 \leq p \leq N, \quad (10)$$

where λ_0 is the maximum among $\lambda_{p,q}$, i.e., $\lambda_0 = \max \lambda_{p,q}$,

$$L^s = \sum_{p=1}^N g'_1(\phi_p), \quad (11)$$

is the Lagrange multiplier to enforce the summation constraint Eq.(1), L_p^c is the Lagrange multiplier to enforce the mass conservation Eq.(3). There is no multiphase conservative Allen-Cahn model available satisfying the summation constraint Eq.(1), mass conservation Eq.(3), and consistency of reduction simultaneously. The difficulty is originated in specifying L_p^c , which is overcome in the present work with the help of the consistent and conservative volume distribution algorithm, see Section 3.2.

2.2.2 Consistent formulation

In order to satisfy the consistency of mass conservation, the Phase-Field equation, either Eq.(7) or Eq.(10), is reformulated in a conservative form using the consistent formulation [28]. Specifically, a set of auxiliary variables $\{Q_p\}_{p=1}^N$ is introduced, whose governing equations are

$$\nabla \cdot (W(\phi_p) \nabla Q_p) = L_p^Q, \quad 1 \leq p \leq N, \quad (12)$$

where

$$W(\phi) = 1 - \phi^2, \quad (13)$$

is the weight function satisfying the consistency of reduction, see [28], and

$$L_p^Q = 0, \quad (14)$$

for the Cahn-Hilliard model Eq.(7), and

$$L_p^Q = -\frac{M_0 \lambda_0}{\eta^2} \left(g'_1(\phi_p) - \frac{1 + \phi_p}{2} L^s \right) + L_p^c, \quad (15)$$

for the conservative Allen-Cahn model Eq.(10). Due to the mass conservation, $(\int_{\Omega} L_p^Q d\Omega)$ is zero for all p . Therefore, Eq.(12) along with the homogeneous Neumann or with the periodic boundary condition is compatible with its source, i.e., the right-hand side (RHS) of Eq.(12), and it is solvable. For convenience, we

use W_p to denote $W(\phi_p)$ in the rest of the paper. As a result, both the Cahn-Hilliard and the conservative Allen-Cahn models can be reformulated into

$$\frac{\partial \phi_p}{\partial t} + \nabla \cdot \mathbf{m}_{\phi_p} = 0, \quad 1 \leq p \leq N, \quad (16)$$

where $\{\mathbf{m}_{\phi_p}\}_{p=1}^N$ are the Phase-Field fluxes, and specifically they are

$$\mathbf{m}_{\phi_p} = \mathbf{u}\phi_p - \sum_{q=1}^N M_{p,q} \nabla \xi_q - W_p \nabla Q_p, \quad 1 \leq p \leq N, \quad (17)$$

for the Cahn-Hilliard model Eq.(7), and

$$\mathbf{m}_{\phi_p} = \mathbf{u}\phi_p - M_0 \lambda_0 \nabla \phi_p - W_p \nabla Q_p, \quad 1 \leq p \leq N, \quad (18)$$

for the conservative Allen-Cahn model Eq.(10).

2.2.3 Momentum equation

The motion of the flow is governed by the momentum equation

$$\frac{\partial(\rho \mathbf{u})}{\partial t} + \nabla \cdot (\mathbf{m} \otimes \mathbf{u}) = -\nabla P + \nabla \cdot (\mu(\nabla \mathbf{u} + \nabla \mathbf{u}^T)) + \rho \mathbf{g} + \mathbf{f}_s, \quad (19)$$

where P is the pressure to enforce the divergence-free condition Eq.(6), \mathbf{g} is the gravity, \mathbf{m} is the consistent mass flux, and \mathbf{f}_s is the surface force due to interfacial tensions between the phases. The definitions of the consistent mass flux and the surface force are

$$\mathbf{m} = \sum_{p=1}^N \frac{\rho_p}{2} (\mathbf{u} + \mathbf{m}_{\phi_p}), \quad (20)$$

$$\mathbf{f}_s = \frac{1}{2} \sum_{p=1}^N \xi_p \nabla \phi_p. \quad (21)$$

The surface force in Eq.(21) is derived from the energy law of the Cahn-Hilliard model in [27], and there are alternative options, e.g., the generalized continuous surface tension force in [38], to model the interfacial tensions.

The momentum equation Eq.(19) also satisfies the consistency of reduction, see the analyses in [27, 28]. With the help of Eq.(4), Eq.(6), Eq.(16) and Eq.(20), It can be easily shown that the density of the fluid mixture and the consistent mass flux satisfy the following mass conservation equation

$$\frac{\partial \rho}{\partial t} + \nabla \cdot \mathbf{m} = 0. \quad (22)$$

Therefore, in addition to the consistency of reduction, both the consistencies of mass conservation and mass and momentum transport are satisfied by the momentum equation Eq.(19).

2.3 Discretizations

The discretizations of all the differential operators follow those in [29]. In summary, we consider the collocated grid arrangement, where all the variables are defined at cell centers, and additional normal velocities are defined at cell faces. The convective operators are approximated by the 5th-order WENO scheme [34], while the other differential operators are discretized by the 2nd-order central difference. To distinguish the discrete operators from their corresponding continuous ones, we add \sim on top of them, e.g., $\tilde{\nabla}$ means the discrete gradient operator. The linear interpolation from the nearest neighbors is denoted by \bar{f} , while any

other approximation of f from its nodal values is denoted as \tilde{f} . The integral is approximated by the mid-point rule, i.e., $\int_{\Omega} f d\Omega \approx \sum_{n_C} [f \Delta\Omega]_{n_C}$, where n_C is the cell index and $\Delta\Omega$ is the cell volume. The time derivative is approximated by $\frac{\gamma_t f^{n+1} - \hat{f}}{\Delta t}$, where f^{n+1} is the value of f at time level $n+1$, Δt is the times step, and γ_t and \hat{f} are scheme dependent. Unless otherwise specified, we use the 2nd-order backward difference to approximate the time derivative, and $\gamma_t = 1.5$ and $\hat{f} = 2f^n - 0.5f^{n-1}$ in this case. $f^{*,n+1}$ is an extrapolation along the time direction and it is $2f^n - f^{n-1}$ for the 2nd-order case.

The numerical scheme for the Cahn-Hilliard model Eq.(7) is the same as that in [27], and the resultant fully-discrete equation is

$$\frac{\gamma_t \phi_p^* - \hat{\phi}_p}{\Delta t} + \tilde{\nabla} \cdot \tilde{\mathbf{m}}_{\phi_p^*} = 0, \quad 1 \leq p \leq N. \quad (23)$$

As analyzed in [27], the scheme guarantees that $\{\phi_p^*\}_{p=1}^N$ satisfies the summation constraint Eq.(1), i.e., $\sum_{p=1}^N \phi_p^* = 2 - N$, the mass conservation Eq.(3), i.e., $\sum_{n_C} [\phi_p^* \Delta\Omega]_{n_C} = \sum_{n_C} [\phi_p^0 \Delta\Omega]_{n_C}$, and the consistency of reduction. We refer interested readers to [27] for detailed descriptions and analyses of the scheme.

The numerical scheme for the conservative Allen-Cahn model Eq.(10) without $\{L_p^c\}_{p=1}^N$ is the same as that in [28]. The first step is to solve the Allen-Cahn equation, i.e., Eq.(10) excluding all the Lagrange multipliers L^s and L_p^c , from

$$\frac{\gamma_t \phi_p^{**} - \hat{\phi}_p}{\Delta t} + \tilde{\nabla} \cdot (\mathbf{u}^{*,n+1} \tilde{\phi}_p^{*,n+1}) = M_0 \lambda_0 \tilde{\nabla} \cdot \tilde{\nabla} \phi_p^{**} - \frac{M_0 \lambda_0}{\eta^2} \tilde{g}'_1(\phi_p^{**}), \quad 1 \leq p \leq N, \quad (24)$$

where $\tilde{g}'_1(\phi_p^{**})$ is the linear approximation of $g'_1(\phi_p^{**})$ from its Taylor expansion at ϕ_p^n . The discrete Lagrange multiplier to enforce the summation constraint Eq.(1) is computed as

$$\tilde{L}^s = \sum_{p=1}^N \left(\tilde{g}'_1(\phi_p^{**}) - \eta^2 \tilde{\nabla} \cdot \tilde{\nabla} \phi_p^{**} \right). \quad (25)$$

Compared to Eq.(11), the appearance of $\tilde{\nabla} \cdot \tilde{\nabla} \phi_p^{**}$ in Eq.(25) is due to $\sum_{p=1}^N \phi_p^{**} \neq 2 - N$. Then the solution is updated from

$$\frac{\gamma_t \phi_p^* - \gamma_t \phi_p^{**}}{\Delta t} = \frac{M_0 \lambda_0}{\eta^2} \frac{1 + \phi_p^n}{2} \tilde{L}^s + \tilde{L}_p^c, \quad 1 \leq p \leq N. \quad (26)$$

The definition of $\{L_p^c\}_{p=1}^N$ and its computation should guarantee that $\{\phi_p^*\}_{p=1}^N$ satisfy the summation constraint Eq.(1), i.e., $\sum_{p=1}^N \phi_p^* = 2 - N$, the mass conservation Eq.(3), i.e., $\sum_{n_C} [\phi_p^* \Delta\Omega]_{n_C} = \sum_{n_C} [\phi_p^0 \Delta\Omega]_{n_C}$, and the consistency of reduction. This will be described in detail in Section 3.2.

It should be noted that $\{\phi_p^*\}_{p=1}^N$, obtained from either Eq.(23) or Eq.(26), are possibly outside their physical interval, i.e., $[-1, 1]$ in the present study, due to either the defect of the model or the numerical error. We finalize the computation of the order parameters by performing the boundedness mapping, which will be elaborated in Section 3.3, to obtain $\{\phi_p^{n+1}\}_{p=1}^N$ from $\{\phi_p^*\}_{p=1}^N$, so that $\{\phi_p^{n+1}\}_{p=1}^N$ not only stay in their physical interval, i.e., $\{\phi_p^{n+1}\}_{p=1}^N \in [-1, 1]$, but also preserve the physical properties. The effect of the boundedness mapping is represented by $\{\tilde{L}_p^b\}_{p=1}^N$, and it is computed from

$$\tilde{L}_p^b = \frac{\gamma_t \phi_p^{n+1} - \gamma_t \phi_p^*}{\Delta t}, \quad 1 \leq p \leq N. \quad (27)$$

Then the consistent formulation is performed discretely, i.e.,

$$\tilde{\nabla} \cdot (\tilde{W}_p^{n+1} \tilde{\nabla} Q_p) = \tilde{L}_p^Q, \quad 1 \leq p \leq N, \quad (28)$$

where

$$\tilde{L}_p^Q = \tilde{L}_p^b, \quad 1 \leq p \leq N, \quad (29)$$

for the Cahn-Hilliard model, and

$$\tilde{L}_p^Q = -\frac{M_0\lambda_0}{\eta^2} \left(\tilde{g}'_1(\phi_p^{**}) - \frac{1+\phi_p^n}{2} \tilde{L}^s \right) + \tilde{L}_p^c + \tilde{L}_p^b, \quad 1 \leq p \leq N, \quad (30)$$

for the conservative Allen-Cahn model. It should be noted that $\{\tilde{L}_p^b\}_{p=1}^N$ are included in $\{\tilde{L}_p^Q\}_{p=1}^N$. After solving $\{Q_p\}_{p=1}^N$, the discrete Phase-Field flux is computed as

$$\tilde{\mathbf{m}}_{\phi_p} = \tilde{\mathbf{m}}_{\phi_p^*} - \overline{W_p^{n+1}} \tilde{\nabla} Q_p, \quad 1 \leq p \leq N, \quad (31)$$

for the Cahn-Hilliard model, and

$$\tilde{\mathbf{m}}_{\phi_p} = \mathbf{u}^{*,n+1} \tilde{\phi}_p^{*,n+1} - M_0\lambda_0 \tilde{\nabla} \phi_p^{**} - \overline{W_p^{n+1}} \tilde{\nabla} Q_p, \quad 1 \leq p \leq N, \quad (32)$$

for the conservative Allen-Cahn model. As a result, the fully-discrete equation of both the Cahn-Hilliard and conservative Allen-Cahn models is

$$\frac{\gamma_t \phi_p^{n+1} - \hat{\phi}_p}{\Delta t} + \tilde{\nabla} \cdot \tilde{\mathbf{m}}_{\phi_p} = 0, \quad 1 \leq p \leq N, \quad (33)$$

which is the discrete counterpart of Eq.(16).

Once $\{\phi_p^{n+1}\}_{p=1}^N$ and $\{\tilde{\mathbf{m}}_{\phi_p}\}_{p=1}^N$ are obtained, the density and viscosity of the fluid mixture are computed from Eq.(4) and Eq.(5), respectively. The discrete mass flux, from Eq.(20), is computed by

$$\tilde{\mathbf{m}} = \sum_{p=1}^N \frac{\rho_p}{2} (\mathbf{u}^{*,n+1} + \tilde{\mathbf{m}}_{\phi_p}). \quad (34)$$

The density and viscosity of the fluid mixture and the discrete mass flux are the input parameters for solving the momentum equation Eq.(19). It should be noted that the consistency of mass conservation is satisfied at the discrete level, thanks to the following discrete mass conservation equation

$$\frac{\gamma_t \rho^{n+1} - \hat{\rho}}{\Delta t} + \tilde{\nabla} \cdot \tilde{\mathbf{m}} = \sum_{p=1}^N \frac{\rho_p}{2} \left(\underbrace{\frac{\gamma_t - \hat{1}}{\Delta t}}_0 + \underbrace{\tilde{\nabla} \cdot \mathbf{u}^{*,n+1}}_0 + \underbrace{\frac{\gamma_t \phi_p^{n+1} - \hat{\phi}_p}{\Delta t} + \tilde{\nabla} \cdot \tilde{\mathbf{m}}_{\phi_p}}_0 \right) = 0, \quad (35)$$

which is the discrete counterpart of Eq.(22), and we have used Eq.(33) and Eq.(36).

The momentum equation Eq.(19) is solved by the scheme in [29] and the divergence-free condition Eq.(6) is enforced on the cell-face velocity, i.e.,

$$\tilde{\nabla} \cdot \mathbf{u} = 0, \quad (36)$$

at all the discrete cells and time levels. This scheme has been successfully applied to two- and multi-phase problems, see [29, 27, 28]. Without the surface force Eq.(21), the momentum of the flow is conserved at the discrete level, i.e., $\sum_{n_C} [\rho \mathbf{u}]_{n_C}^n = \sum_{n_C} [\rho \mathbf{u}]_{n_C}^0$. The surface force Eq.(21) can be discretized by either the balanced-force method, which achieves better numerical force balance, or the conservative method, which fully conserves the momentum [27]. Inside the bulk-phase regions, the single-phase Navier-Stokes equation with the corresponding phase density and viscosity is exactly recovered by the fully-discrete momentum equation. In addition, it can be shown that the consistency conditions are satisfied at the discrete level by the scheme. The analyses of the scheme for the momentum equation are performed in detail in [29, 27, 28].

3 The consistent and conservative volume distribution algorithm and its applications

In this section, the consistent and conservative volume distribution algorithm is described in detail. Then, its applications to the Phase-Field models are introduced.

3.1 The consistent and conservative volume distribution algorithm

The purpose of the algorithm is to specify the volumes of individual phases to be distributed at every location of the domain, denoted as $\{L_p\}_{p=1}^N$, in a consistent and conservative manner. The inputs of the algorithm are the total volumes of individual phases to be distributed in the domain, denoted as $\{S_p\}_{p=1}^N$, and a set of order parameters $\{\phi_p\}_{p=1}^N$. The algorithm only distributes the volumes, while it does not change the total volume of the domain. Therefore, $\{S_p\}_{p=1}^N$ are admissible only if they satisfy the summation constraint for global volume distribution, i.e.,

$$\sum_{p=1}^N S_p = 0. \quad (37)$$

There are multiple choices for $\{L_p\}_{p=1}^N$ with given $\{S_p\}_{p=1}^N$, while not all of them are admissible. We propose three constraints that should be strictly satisfied by $\{L_p\}_{p=1}^N$.

The first constraint is the summation constraint for local volume distribution. Since the summation constraint for the order parameters Eq.(1) should be preserved before and after the volume distribution everywhere in the domain, the admissible $\{L_p\}_{p=1}^N$ should have the following property

$$\sum_{p=1}^N L_p = 0. \quad (38)$$

Eq.(38) grants that no local void or overfill can be generated by the volume distribution algorithm.

The second constraint is the conservation constraint for volume distribution, i.e.,

$$\int_{\Omega} L_p d\Omega = S_p, \quad 1 \leq p \leq N. \quad (39)$$

It should be noted that Eq.(39) is consistent with Eq.(37) and Eq.(38), when Eq.(39) is summed over all the p .

The last constraint is the consistency of reduction. There should be no fictitious phases generated after the volume distribution. Based on the given order parameters $\{\phi_p\}_{p=1}^N$, there should not be any volume of phase p being distributed to where phase p is absent, i.e, $\phi_p = -1$. Therefore, it requires

$$L_p|_{\phi_p=-1} = 0, \quad 1 \leq p \leq N. \quad (40)$$

If $\phi_p = 1$ at a specific location, then the order parameters of the other phases are -1 at the same location from the summation constraint for the order parameters Eq.(1). Combining Eq.(38) and Eq.(40), we can obtain $L_p|_{\phi_p=1} = 0$. In other words, the volume distribution only happens at the interfacial regions, while it is deactivated inside the bulk-phase regions.

If $\{L_p\}_{p=1}^N$ satisfy all the aforementioned constraints, then they are consistent and conservative. A successful algorithm is developed in [28] for two-phase flows. However, it is far more challenging in a general multiphase case. In a two-phase case, the phases inside the interfacial regions are always fixed and the volume distribution problem is solved phase-wise, since we only need to consider one of the phases and the other phase is automatically obtained from the summation constraint for the local volume distribution Eq.(38). In a general multiphase case, there are lots of different possible combinations of the phases inside the interfacial regions, and the volume change of one of the phases is unable to directly or uniquely determine those of the other phases from Eq.(38).

Due to the complexity of including multiple phases, the volume distribution is unable to be performed phase-wise. A general form of volume distribution is

$$L_p = \sum_{q=1}^N W_{p,q} B_q, \quad 1 \leq p \leq N, \quad (41)$$

where $W_{p,q}$ is the weight function for volume distribution and should be non-zero only in the interfacial regions including phases p and q from the consistency of reduction, and B_p conceptually is related to the

total volume of phase p to be distributed. Eq.(41) can be understood as following. B_q , which is related to the total volume of phase q to be distributed in the domain, can only be distributed to the interfacial regions including phase q . Therefore, the volume distributed to the interfacial regions including both phases p and q from B_q is $W_{p,q}B_q$. Then we sum all the contributions from the phases and obtain $\{L_p\}_{p=1}^N$.

Based on the consistency of reduction, we construct the weight function for volume distribution to be

$$W_{p,q} = \begin{cases} -(1 + \phi_p)(1 + \phi_q), p \neq q, \\ (1 + \phi_p)(1 - \phi_q), p = q, \end{cases} \quad 1 \leq p, q \leq N, \quad (42)$$

so that Eq.(40) is satisfied. It should be noted that $W_{p,q}$ is non-zero only at the interfacial regions including phases p and q , i.e., where $-1 < \phi_p, \phi_q < 1$. Therefore, $W_{p,q}$ indicates the interfacial regions including both phases p and q .

The summation constraint for local volume distribution Eq.(38) becomes

$$\sum_{p=1}^N W_{p,q} = 0, \quad (43)$$

and it is satisfied based on the definition of $W_{p,q}$ in Eq.(42), as long as Eq.(1), i.e., $\sum_{p=1}^N \phi_p = 2 - N$, is satisfied.

The conservation constraint for volume distribution Eq.(39) becomes

$$\sum_{q=1}^N \left(\int_{\Omega} W_{p,q} d\Omega \right) B_q = S_p, \quad 1 \leq p \leq N, \quad (44)$$

which is a linear system for $\{B_p\}_{p=1}^N$. The coefficient matrix of the linear system is the integral of the weight function $W_{p,q}$ over the domain. Since $W_{p,q}$ is symmetric, the coefficient matrix is symmetric as well. Another observation is that all the diagonal elements of the coefficient matrix are positive while all the off-diagonal elements are negative. In addition, the summation of each row is zero, which implies that the summation of the absolute value of the off-diagonal elements in a row equals the diagonal element of the row. As a result, the coefficient matrix is diagonally dominant. Our implementations show that solving Eq.(44) following the scaling argument below is critical for the success of the algorithm. It should be noted that $\{W_{p,q}\}_{p,q=1}^N$ are on $O(1)$. Suppose the domain considered also has a size on $O(1)$, the magnitude of $\{B_p\}_{p=1}^N$ should be on $O(\{S_p\}_{p=1}^N)$ from Eq.(44). Another important observation from Eq.(44) is that the rank of the coefficient matrix is at most $N - 1$. When we sum Eq.(44) over all the p , we obtain zeros on both sides of the equation due to Eq.(43) on the left-hand side (LHS) and to Eq.(37) on the right-hand side (RHS). As a result, Eq.(44) has multiple solutions and the scaling argument should be the criteria to specify the admissible one, especially when $\{S_p\}_{p=1}^N$ are close to the round-off error. A robust way to employ the scaling argument is to let B_{p^*} equal to $\max_p |S_p|$, where p^* is the column index of the column including the minimum absolute value other than zero of all the elements of the coefficient matrix. Consequently, Eq.(44) has a unique solution that honors the scaling argument. A special case is when there is a phase, e.g., phase p , doesn't have interfacial regions in the whole domain. Equivalently, phase p is either absent, i.e., $\phi_p \equiv -1$, or filling the whole domain, i.e., $\phi_p \equiv 1$. As a result, both the p th row and column in the coefficient matrix are zero, and we set $B_p = 0$ when this happens. In practice, the coefficient matrix in Eq.(44) is rescaled by the maximum absolute value among its elements, if that value is not zero, and correspondingly $\{W_{p,q}\}_{p,q=1}^N$ are rescaled by that value. As a result, the coefficient matrix is always on $O(1)$, independent of the domain size. In numerical implementations, all the integrals are approximated by the mid-point rule, like those mentioned in Section 2.3. Once $\{B_p\}_{p=1}^N$ are solved, the volume distributions for individual phases are obtained from Eq.(41).

Here, we consider a special case where there are only two phases. Therefore, we have $\phi_1 = -\phi_2$ and $S_1 = -S_2$ due to their summation constraints. From Eq.(44), we obtain the following equations

$$\begin{cases} S_1 = B_1 \int_{\Omega} W_{1,1} d\Omega + B_2 \int_{\Omega} W_{1,2} d\Omega = (B_1 - B_2) \int_{\Omega} (1 - \phi_1^2) d\Omega = (B_1 - B_2) \int_{\Omega} W_1 d\Omega \\ S_2 = B_1 \int_{\Omega} W_{2,1} d\Omega + B_2 \int_{\Omega} W_{2,2} d\Omega = -(B_1 - B_2) \int_{\Omega} (1 - \phi_2^2) d\Omega = -(B_1 - B_2) \int_{\Omega} W_2 d\Omega \end{cases} \quad (45)$$

and it should be noted that the above two equations are identical due to $S_1 = -S_2$, $\phi_1 = -\phi_2$, and $W_1 = W_2$. Finally from Eq.(41), we obtain

$$\begin{cases} L_1 = B_1 W_{1,1} + B_2 W_{1,2} = (B_1 - B_2)(1 - \phi_1^2) = \frac{W_1}{\int_{\Omega} W_1 d\Omega} S_1, \\ L_2 = B_1 W_{2,1} + B_2 W_{2,2} = -(B_1 - B_2)(1 - \phi_2^2) = \frac{W_2}{\int_{\Omega} W_2 d\Omega} S_2. \end{cases} \quad (46)$$

Therefore, the volume distribution algorithm becomes phase-wise in two-phase cases.

In summary, a consistent and conservative volume distribution for multiple phases is developed. The complexity for multiphase cases originates in simultaneously satisfying the three physical constraints for volume distribution, which are the summation constraint Eq.(38), the conservation constraint Eq.(39), and the consistency of reduction Eq.(40). Therefore, the volume distribution is unable to be performed phase-wise, like the two-phase case, but has to consider the contributions from different phases altogether.

3.2 L_p^c in the conservative Allen-Cahn model

The solution of the conservative Allen-Cahn model Eq.(10) should satisfy the summation constraint for the order parameters Eq.(1), the mass conservation Eq.(3), and the consistency of reduction.

In order to satisfy the summation constraint for the order parameters Eq.(1), both the left- and right-hand sides of the equation should be zero after summing Eq.(10) over all the p . This requires

$$\sum_{p=1}^N L_p^c = 0. \quad (47)$$

The mass conservation Eq.(3) requires

$$\int_{\Omega} L_p^c d\Omega = \int_{\Omega} \frac{M_0 \lambda_0}{\eta^2} \left(g'_1(\phi_p) - \frac{1 + \phi_p}{2} L^s \right) d\Omega = S_p^c, \quad 1 \leq p \leq N, \quad (48)$$

where $\sum_{p=1}^N S_p^c = 0$ from the definition of L^s in Eq.(11). Finally, from the consistency of reduction, the phase, e.g., phase p , which is absent at $t = 0$, i.e., $\phi_p|_{t=0} \equiv -1$, should not appear, i.e., $\phi_p \equiv -1$ at $\forall t > 0$. Therefore, it requires

$$L_p^c|_{\phi_p=-1} = 0, \quad 1 \leq p \leq N. \quad (49)$$

It is obvious that the constraints for $\{L_p^c\}_{p=1}^N$ are the same as those for $\{L_p\}_{p=1}^N$ in Section 3.1. Therefore, the consistent and conservative volume distribution algorithm in Section 3.1 is directly applied to specify $\{L_p^c\}_{p=1}^N$.

It should be noted that, in the two-phase case, $L^s = 0$ and $\{L_p^c\}_{p=1}^2$, from Section 3.1, are

$$L_p^c = \frac{W_p}{\int_{\Omega} W_p d\Omega} S_p^c, \quad p = 1, 2.$$

As a result, the multiphase conservative Allen-Cahn model proposed in the present work exactly recovers the two-phase conservative Allen-Cahn model proposed by Brassel and Bretin [7], further studied in [41, 44], and later on applied to two-phase flows [33, 36, 35, 28].

Kim and Lee [40] developed a similar conservative Allen-Cahn model for multiphase flows. The only difference from the present work is that they defined $\{L_p^c\}_{p=1}^N$ as

$$L_p^c = \frac{\sum_{q=1}^N W_q}{\sum_{q=1}^N \int_{\Omega} W_q d\Omega} S_p^c, \quad 1 \leq p \leq N. \quad (50)$$

Although $\{L_p^c\}_{p=1}^N$ defined in Eq.(50) satisfy Eq.(47) and Eq.(48), they are not reduction consistent, i.e., violating Eq.(49). As a result, fictitious phases can be generated by their model. For example, at an interfacial region of phases p and q only, i.e., $-1 < \phi_p, \phi_q < 1$, phase r ($r \neq p, q$) should be absent, i.e.,

$\phi_r = -1$. Therefore, $\sum_{m=1}^N W_m$ is positive and non-zero. If S_r^c is again positive, then from Eq.(50), L_r^c is positive, which means phase r is being generated at the interfacial regions only including phases p and q . On the other hand, ϕ_r will be less than -1 if S_r^c is negative. Neither of the results is physical. Since S_r^c is a global term, i.e., obtained from an integral over the domain, we shall not expect it to be zero except that ϕ_r is 1 or -1 everywhere. However, these two cases are meaningless in practice since they restrict the problem to be single- or two-phase.

Correspondingly at the discrete level, $\{\tilde{L}_p^c\}_{p=1}^N$, which is approximating $\{L_p^c\}_{p=1}^N$, are obtained from the consistent and conservative volume distribution algorithm in Section 3.1, and have the following properties

$$\sum_{p=1}^N \tilde{L}_p^c = 0, \quad (51)$$

$$\sum_{n_C} [\tilde{L}_p^c \Delta \Omega]_{n_C} = \sum_{n_C} \left[\frac{M_0 \lambda_0}{\eta^2} \left(\tilde{g}'_1(\phi_p^{**}) - \frac{1 + \phi_p^n}{2} \tilde{L}^s \right) \Delta \Omega \right]_{n_C}, \quad 1 \leq p \leq N, \quad (52)$$

$$\tilde{L}_p^c|_{\phi_p^n = -1} = 0, \quad 1 \leq p \leq N. \quad (53)$$

Along with \tilde{L}^s in Eq.(25), we can show that $\{\phi_p^*\}_{p=1}^N$ obtained from the proposed scheme, i.e., Eq.(24) and Eq.(26), satisfy the summation constraint for the order parameters, the mass conservation, and the consistency of reduction at the discrete level.

Suppose the summation constraint for the order parameters Eq.(1) is true at every cell up to time level n , summing Eq.(24) and Eq.(26) together then summing the resultant equation over all the p , we have $\sum_{p=1}^N \phi_p^* = \sum_{p=1}^N \phi_p / \gamma_t = (\widehat{2 - N}) / \gamma_t = (2 - N)$ from Eq.(51), Eq.(25), and $\hat{1} = \gamma_t$. Therefore, the summation constraint for the order parameters Eq.(1) is true at every cell and every time level. It should be noted that we have applied the correction step for the convection term in Eq.(24) with the gradient-based phase selection, proposed in [27], so that the consistency of reduction is not influenced, and, at the same time, $\sum_{p=1}^N \tilde{\nabla} \cdot (\mathbf{u}^{*,n+1} \tilde{\phi}_p^{*,n+1}) = \tilde{\nabla} \cdot (\mathbf{u}^{*,n+1} (2 - N)) = (2 - N) \tilde{\nabla} \cdot \mathbf{u}^{*,n+1} = 0$ is true. Otherwise, either the summation constraint for the order parameters Eq.(1) can be violated or fictitious phases can be generated numerically, which has been demonstrated in [27].

Suppose the mass conservation Eq.(3) is satisfied at the discrete level up to time level n , i.e., $\sum_{n_C} [\phi_p^n \Delta \Omega]_{n_C} = \sum_{n_C} [\phi_p^0 \Delta \Omega]_{n_C}$ for all p , summing Eq.(24) and Eq.(26) together, multiplying the resultant equation by $\Delta \Omega$, then summing it over all the cells, we have $\sum_{n_C} [\phi_p^* \Delta \Omega]_{n_C} = \sum_{n_C} [\widehat{\phi_p \Delta \Omega}]_{n_C} / \gamma_t = \sum_{n_C} [\widehat{\phi_p^0 \Delta \Omega}]_{n_C} / \gamma_t = \sum_{n_C} [\phi_p^0 \Delta \Omega]_{n_C}$ for all p from Eq.(52). Therefore, the mass conservation is satisfied at every time level for all the phases. The proof of $\sum_{n_C} [\tilde{\nabla} \cdot \mathbf{f}]_{n_C} = 0$ for an arbitrary vector function \mathbf{f} is available in [27].

Suppose phase p is absent at $t = 0$, i.e., $\phi_p|_{t=0} = -1$, and it is absent up to time level n , $\phi_p^{**} = -1$ is the solution of Eq.(24) by noticing that $g'_1(-1) = 0$, $\tilde{\phi}_p^{*,n+1} = -1$, and $\hat{\phi}_p = -\gamma_t$. Thanks to Eq.(53), we obtain $\phi_p^* = -1$ from Eq.(26). For other phases, e.g., phase r , Eq.(24) is not influenced since it only depends on phase r . \tilde{L}^s in Eq.(25) becomes $\sum_{q=1, q \neq p}^N \left(\tilde{g}'_1(\phi_q^{**}) - \eta^2 \tilde{\nabla} \cdot \tilde{\nabla} \phi_q^{**} \right)$ by noticing that both $\tilde{g}'_1(\phi_p^{**})$ and $\tilde{\nabla} \cdot \tilde{\nabla} \phi_p^{**}$ are zero. As discussed in Section 3.1, the absence of phase p results in $\tilde{L}_r^c = \sum_{q=1, q \neq p}^N W_{r,q} B_q$ since both B_p and $W_{r,p}$ are zero. As a result, phase p remains absent and the other phases are updated without any influences from phase p . In other words, the N -phase model reduces to the corresponding $(N - 1)$ -phase model automatically. Therefore, the consistency of reduction is satisfied discretely.

It is suggested in [45] that the term $\frac{1+\phi_p}{2}$ ahead of L^s in Eq.(10) is replaced by $\left(\frac{1+\phi_p}{2} \right)^{\gamma_s}$, where γ_s is larger than 1, in order to reduce the amounts of fictitious phases. The numerical results in [45] indicate that by increasing γ_s by 1, the peak of the fictitious phase is about two orders of magnitude smaller. However, we have shown in this section that both the proposed conservative Allen-Cahn model using $\frac{1+\phi_p}{2}$ ahead of L^s and its numerical scheme are not going to generate any fictitious phases, which will be demonstrated in Section 4. With the same procedure of analysis, choosing $\left(\frac{1+\phi_p}{2} \right)^{\gamma_s}$ ($\gamma_s \geq 1$) ahead of L^s in Eq.(10) does

not change the consistency of reduction of the proposed conservative Allen-Cahn model and its numerical scheme. The reason for generating fictitious phases in [45] is that the scheme in [45] doesn't satisfy the consistency of reduction. In previous studies, e.g., [13, 14, 15, 16, 38, 45, 40], only the first $(N - 1)$ order parameters are solved from the Phase-Field equation numerically and the N th one is computed from the summation constraint, i.e., Eq.(1). Although the summation constraint, i.e., Eq.(1), is satisfied, the consistency of reduction can be easily violated. For example, we have a three-phase system where phase 3 is absent. Consequently, the exact solution of the order parameters should satisfy the following properties: $\phi_1^E + \phi_2^E + \phi_3^E = -1$ and $\phi_3^E = -1$, everywhere. If only the first two order parameters are solved from the Phase-Field equation independently, there is no guarantee that the summation of the numerical solutions of phases 1 and 2 is zero, i.e., $\phi_1 + \phi_2 = 0$, everywhere, especially at the interfacial regions where the gradients of ϕ_1 and ϕ_2 are large. Then, $\phi_3 = -1 - (\phi_1 + \phi_2) \neq -1$. In other words, phase 3 is unphysically generated by the scheme. On the other hand, the proposed schemes for both the multiphase Cahn-Hilliard and conservative Allen-Cahn models solve all the order parameters. The consistency of reduction of the schemes ensures that $\phi_3 = -1$ after solving the equation for phase 3, and the summation constraint, i.e., Eq.(1), ensures that $\phi_1 + \phi_2 + \phi_3 = 0$. Consequently, no Phase 3 is being generated and $\phi_1 + \phi_2 = 0$ is valid everywhere by the proposed schemes.

In summary, with the help of the consistent and conservative volume distribution algorithm to specify $\{L_p^c\}_{p=1}^N$, we develop a multiphase conservative Allen-Cahn model that satisfies the summation constraint for the order parameters Eq.(1), the mass conservation Eq.(3), and the consistency of reduction, simultaneously. At the best of the authors' knowledge, this is the first multiphase conservative Allen-Cahn model that achieves these properties. A corresponding numerical scheme is developed for the multiphase conservative Allen-Cahn model. The solution from the scheme preserves the aforementioned physical properties of the model at the discrete level. Therefore, the scheme is consistent and conservative.

3.3 The boundedness mapping

It is always expected that the order parameters are bounded by a specific interval, i.e., $[-1, 1]$ in the present work. Otherwise, there is no physical interpretation for a volume fraction larger than 1 or below 0. When there is a significant difference among the material properties, negative density or viscosity can be generated even though the out-of-bound error is small. As a result, the governing equations become ill-posed. However, either the defect of the model or the numerical error contributes to the out-of-bound solutions of the order parameters. In this section, we introduce a numerical procedure, called the boundedness mapping, to address the out-of-bound solution while the physical properties of the solution remain intact. As an example, we consider its application to the proposed multiphase Cahn-Hilliard and conservative Allen-Cahn models, although it can be applied to many other multiphase models.

Suppose $\{\phi_p^*\}_{p=1}^N$ are obtained from either Eq.(23) or Eq.(26), and they satisfy the summation constraint for the order parameters, the mass conservation, and the consistency of reduction at the discrete level, as shown in Section 3.2 and in [27]. We need to specify a mapping from $\{\phi_p^*\}_{p=1}^N$ to $\{\phi_p^{n+1}\}_{p=1}^N$ so that $\{\phi_p^{n+1}\}_{p=1}^N$ preserve all the aforementioned properties of $\{\phi_p^*\}_{p=1}^N$ and, in addition, $\{\phi_p^{n+1}\}_{p=1}^N \in [-1, 1]$.

The first step is clipping the out-of-bound value, i.e.,

$$\phi_p^{b*} = \begin{cases} 1, \phi_p^* \geq 1, \\ -1, \phi_p^* \leq -1, \\ \phi_p^*, \text{ else.} \end{cases} \quad (54)$$

It should be noted that the clipping step Eq.(54) is only effective in the interfacial regions. As shown in Section 3.2 and in [27], $\{\phi_p^*\}_{p=1}^N$ are either 1 or -1 inside bulk-phase regions, thanks to the consistency of reduction. As a result, the out-of-bound solutions are only possible to first appear at interfacial regions. Since the clipping step Eq.(54) doesn't modify any existing bulk-phase regions labeled by $\{\phi_p^*\}_{p=1}^N$ and $\{\phi_p^*\}_{p=1}^N$ are reduction consistent, $\{\phi_p^{b*}\}_{p=1}^N$ preserves the consistency of reduction and no fictitious phases are generated after the clipping step.

The next step is the rescaling step to enforce the summation constraint for the order parameters without changing the consistency of reduction. We first specify a provisional volume fraction from Eq.(2) using

$\{\phi_p^{b*}\}_{p=1}^N$. Then we rescale the volume fractions by $\sum_{p=1}^N C_p^{b*}$, i.e.,

$$C_p^{b**} = \frac{C_p^{b*}}{\sum_{p=1}^N C_p^{b*}}. \quad (55)$$

Therefore, we have $\sum_{p=1}^N C_p^{b**} = 1$. The consistency of reduction is preserved since $C_p^{b**}|_{\phi_p^* \leq -1} = 0$. Then we invert the volume fractions $\{C_p^{b**}\}_{p=1}^N$ by $\{\phi_p^{b**} = 2C_p^{b**} - 1\}_{p=1}^N$. Now $\{\phi_p^{b**}\}_{p=1}^N$ satisfy the summation constraint for the order parameters, i.e., $\sum_{p=1}^N \phi_p^{b**} = 2 - N$, the consistency of reduction, i.e., $\phi_p^{b**}|_{\phi_p^* \leq -1} = -1$ for all p , and the boundedness constraint, i.e., $\{\phi_p^{b**}\}_{p=1}^N \in [-1, 1]$. Again, no fictitious phases are generated after the rescaling step.

The remaining constraint is the mass conservation and we perform the conservation step, i.e.,

$$\phi_p^{n+1} = \phi_p^{b**} + \mathcal{L}_p^b. \quad (56)$$

To preserve the summation constraint for the order parameters by $\{\phi_p^{n+1}\}_{p=1}^N$, it requires

$$\sum_{p=1}^N \mathcal{L}_p^b = 0. \quad (57)$$

To preserve the mass conservation, it requires

$$\sum_{n_C} [\mathcal{L}_p \Delta \Omega]_{n_C} = \sum_{n_C} [(\phi_p^{n+1} - \phi_p^{b**}) \Delta \Omega]_{n_C} = \sum_{n_C} [(\phi_p^* - \phi_p^{b**}) \Delta \Omega]_{n_C} = S_p^b, \quad 1 \leq p \leq N. \quad (58)$$

To preserve the consistency of reduction, it requires

$$\mathcal{L}_p^b|_{\phi_p^{b**} = -1} = 0, \quad 1 \leq p \leq N. \quad (59)$$

It is obvious that the constraints for $\{\mathcal{L}_p^b\}_{p=1}^N$ are the same as those for $\{L_p\}_{p=1}^N$ in Section 3.1. Therefore, the consistent and conservative volume distribution is applied to specified $\{\mathcal{L}_p^b\}_{p=1}^N$. Although Eq.(56) doesn't explicitly guarantee the boundedness constraint, i.e., $\{\phi_p^{n+1}\}_{p=1}^N \in [-1, 1]$, we can iteratively apply the procedure in this section by replacing $\{\phi_p^*\}_{p=1}^N$ with $\{\phi_p^{n+1}\}_{p=1}^N$ obtained from Eq.(56) until the boundedness constraint is achieved. From Eq.(56), the out-of-bound solution is most probably where $|\phi_p^{b**}|$ is close to one, since $\mathcal{L}_p^b|_{\phi_p^{b**} = \pm 1} = 0$ for all p and $\{\phi_p^{b**}\}_{p=1}^N$ are bounded. However, at those locations, $W_{p,q}$ defined in Eq.(42) is close to zero. In addition, the out-of-bound error introduced by $\{\phi_p^*\}_{p=1}^N$ is normally small. The largest out-of-bound error observed is usually on $O(10^{-5})$ in one time step. Therefore we never observe any necessity for iteration in our numerical practices even in the problems including strong interactions among phases. Once $\{\phi_p^{n+1}\}_{p=1}^N$ are obtained, $\{\mathcal{L}_p^b\}_{p=1}^N$ are computed as Eq.(27).

Consider a location where $\phi_p^* = -1$. From the clipping step, $\phi_p^{b*} = -1$. Therefore, both C_p^{b*} and C_p^{b**} are zero and ϕ_p^{b**} is again -1 after the rescaling step. Thanks to Eq.(59) in the conservation step, finally we obtain $\phi_p^{n+1} = \phi_p^* = -1$ from Eq.(56). In other words, phase p remains absent at where $\phi_p^* = -1$. This eliminates any generation of fictitious phases due to the boundedness mapping. The contributions of ϕ_p^* to the clipping Eq.(54), rescaling Eq.(55), and conservation steps Eq.(56) are all zero. As a result, the boundedness mapping is reduction consistent. Therefore, the consistency of reduction of $\{\phi_p^*\}_{p=1}^N$ is preserved by $\{\phi_p^{n+1}\}_{p=1}^N$ obtained from the boundedness mapping. Following the analysis in Section 3.1 to the two-phase case, it should be noted that the proposed boundedness mapping exactly reduces to the one in [28] for two-phase flows.

In summary, $\{\phi_p^{n+1}\}_{p=1}^N$, which is obtained from $\{\phi_p^*\}_{p=1}^N$ with the boundedness mapping, preserves the summation constraint for the order parameters, i.e., $\sum_{p=1}^N \phi_p^{n+1} = 2 - N$, the mass conservation, i.e., $\sum_{n_C} [\phi_p^{n+1} \Delta \Omega]_{n_C} = \sum_{n_C} [\phi_p^0 \Delta \Omega]_{n_C}$ for all p , and the consistency of reduction, and additionally satisfy the boundedness constraint, i.e., $\{\phi_p^{n+1}\}_{p=1}^N \in [-1, 1]$. In conclusion, the proposed schemes for both the multiphase Cahn-Hilliard and conservative Allen-Cahn models are consistent, conservative, and bounded.

4 Results

In this section, various numerical tests are performed to validate the properties of the Phase-Field models and their schemes, including the applications of the consistent and conservative volume distribution algorithm, and to demonstrate their capability in multiphase flows. For brevity, we use CH and CAC to denote the multiphase Cahn-Hilliard and conservative Allen-Cahn models, respectively. If the boundedness mapping is supplemented, those models are denoted by CHB and CACB. We use h to denote the grid/cell size.

4.1 Fictitious phases

To illustrate the importance of satisfying the consistency of reduction, we compare the numerical equilibrium state of the Phase-Field models without coupling to the flow, i.e., $\mathbf{u} \equiv \mathbf{0}$. In addition to CH, CHB, CAC, and CACB, the multiphase conservative Allen-Cahn model, proposed in [40], is supplemented, and it is called CACN in this case. As analyzed in Section 3.2, CACN is not reduction consistent and can generate fictitious phases.

The domain considered is $[1 \times 1]$ with homogeneous Neumann boundaries. The domain is discretized by $[128 \times 128]$ cells and the time step is $\Delta t = 10h$. We set $\eta = 0.015$ and the off-diagonal elements of $\lambda_{p,q}$ are $\frac{3}{2\sqrt{2}}\eta$. M_0 is (η^2/λ_0) for CAC, CACB, and CACN, and is $10^{-3}\eta^2$ for CH and CHB due to numerical stability. The circle of phase 1 is at $(0.25, 0.25)$ with a radius 0.1. The circle of phase 2 is at $(0.5, 0.75)$ with a radius 0.1. The circle of phase 3 is at $(0.75, 0.25)$ with a radius 0.1. Phase 4 occupies the rest of the domain. The circles of Phases 1, 2, and 3 are separated far enough, so there are no intersections among them. Therefore, $\eta^3|\nabla\phi_1||\nabla\phi_2||\nabla\phi_3|$ should be zero.

Fig.1 shows the equilibrium profiles from different Phase-Field models, along with $\eta^3|\nabla\phi_1||\nabla\phi_2||\nabla\phi_3|$. It can be observed from Fig.1 **a)** that some amounts of phase 1 from CACN are generated at the interfacial regions of phases 2 and 4, and of phases 3 and 4. Phases 2 and 3 from CACN behave similarly to phase 1. More clearly, $\eta^3|\nabla\phi_1||\nabla\phi_2||\nabla\phi_3|$ is non-zero at all the interfacial regions. Unphysically generating fictitious phases is because CACN violates the consistency of reduction, as analyzed in Section 3.2. On the other hand, the results from CH, CHB, CAC, and CACB do not generate any fictitious phases, and $\eta^3|\nabla\phi_1||\nabla\phi_2||\nabla\phi_3|$ from those models is machine zero, since the consistency of reduction is satisfied by those models and their schemes. In addition, there is little difference in the profiles from CH, CHB, CAC, and CACB.

4.2 Under-resolved structures

The comparison study in [44] shows that the two-phase CAC has a better ability to preserve under-resolved structures than CH. Here, we perform the multiphase version of that study and consider CH, CHB, CAC, and CACB. Again, the velocity is set to be zero, i.e., $\mathbf{u} \equiv \mathbf{0}$.

The domain considered is $[1 \times 1]$ with homogeneous Neumann boundaries. The number of cells to discretize the domain is $[128 \times 128]$ and the time step is $\Delta t = 10h$. We set $\eta = h$, $M_0 = 10^{-3}\eta^2$, and the off-diagonal elements of $\lambda_{p,q}$ are $\frac{3}{2\sqrt{2}}\eta$. Phase 1 is enclosed by a circle at $(0.5, 0.5)$ with a diameter 0.2. Phase 2 is enclosed by a circle at $(0.2, 0.2)$ with a diameter 0.1. Phase 3 is enclosed by a circle at $(0.8, 0.8)$ with a diameter 0.05. Phase 4 occupies the rest of the domain.

The number of grid points across the circles, i.e., D/h , is 25.6 for phase 1, 12.8 for phase 2, and 6.4 for phase 3. If the interfacial region is defined as $-0.995 < \phi < 0.995$, the number of grid points across the interfacial region is $n_I = 2\sqrt{2}\tanh^{-1}(0.995)\eta/h \approx 8.5$. Therefore, about 17 grid points across the circle of phase 1 are inside the bulk-phase region of phase 1. Inside the bulk-phase region of phase 2, there are 5 grid points across the circle of phase 2, while there is none inside the bulk-phase region of phase 3. We quantify the evolution of individual circles by measuring their diameters for a long period of time, and the results are shown in Fig.2. It is clear that the diameter of the smallest circle (phase 3) decreases and it finally disappears at about $t = 750$ for CH and CHB. Correspondingly, the maximum of ϕ_3 becomes less than zero. The shrinkage of the other two circles is negligible, considering the long period of simulation time. On the other hand, all the circles are preserved and their diameter does not change with time for CAC and CACB. The maximum ϕ_3 less than 1 at $t = 0$ represents the poor resolution of the smallest circle that there is no bulk-phase region of phase 3 at the beginning. Nevertheless, unlike CH and CHB, both CAC and CACB preserve this under-resolved structure very well.

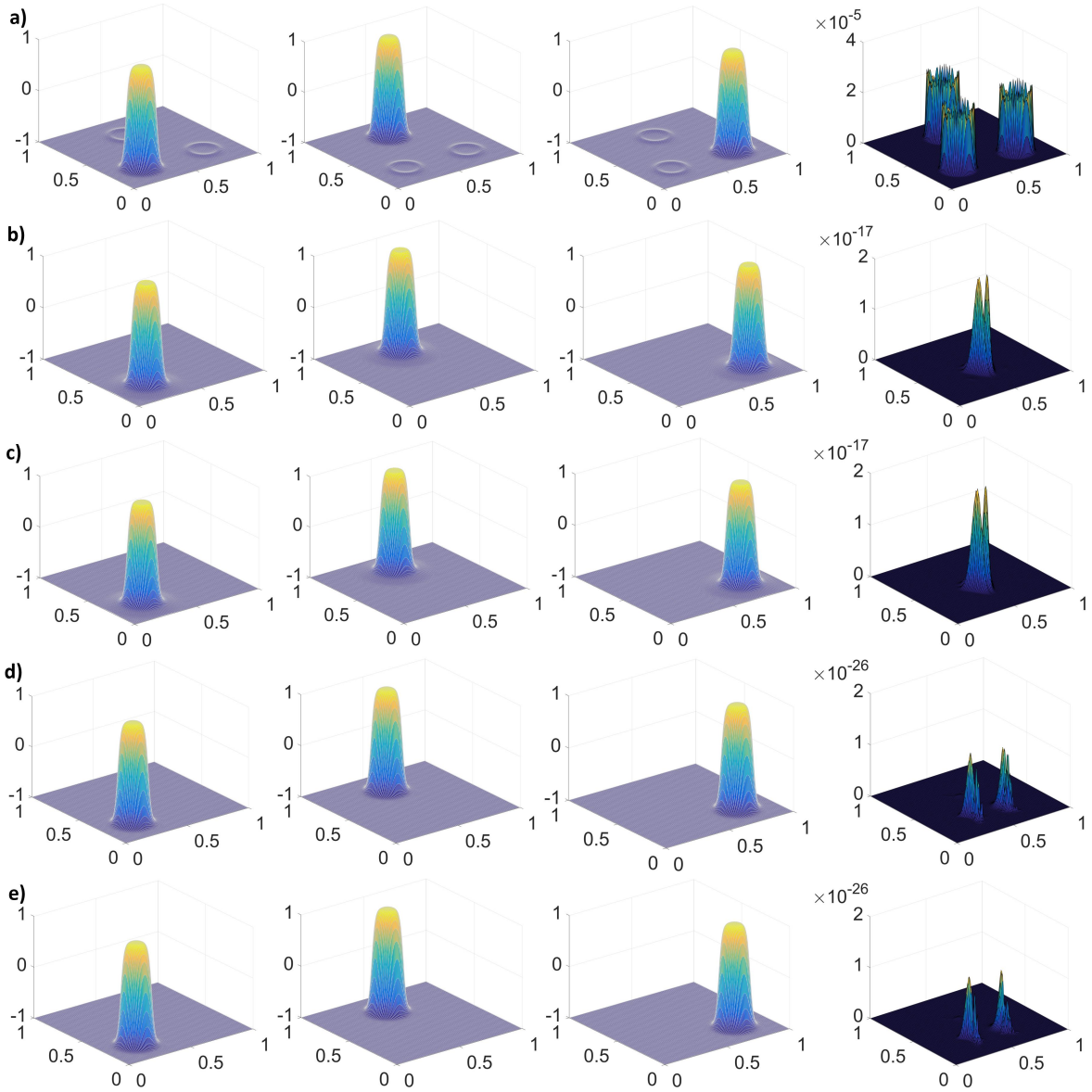


Figure 1: Results of the fictitious phases from a) CACN, b) CH, c) CHB, d) CAC, and e) CACB. The first column: Profile of phase 1. The second column: Profile of phase 2. The third column: Profile of phase 3. The fourth column: $\eta^3 |\nabla \phi_1| |\nabla \phi_2| |\nabla \phi_3|$.

Without the boundedness mapping, the result using CH becomes unstable after the smallest circle disappears, i.e., $\max \phi_3 < 0$. We can observe that the maximum of ϕ_2 is larger than 1 and increases with a dramatic rate. Due to the summation constraint for the order parameters, the minimum of ϕ_4 decreases beyond -1 with similar behavior. We can infer that the out-of-bound error appears at the interfacial region between phases 2 and 4. Fig.3 **a)** shows the profiles of ϕ_2 at selected moments from CH. At the interfacial region of phases 2 and 4, an out-of-bound error initializes, which is consistent with the analysis in Section 3.3. As time goes on, the out-of-bound error keeps growing and becomes a spike. As a result, the profile of ϕ_2 is significantly contaminated and becomes unphysical. Eventually, numerical instability is triggered due to the large out-of-bound error. We supplement the profiles of ϕ_2 using CHB at the same moments in Fig.3 **b)**. Thanks to the boundedness mapping, the out-of-bound error is eliminated. Consequently, the physical profile of ϕ_2 is preserved and the computation is stable. The out-of-bound error from CAC is on the order of the round-off error. Thus, the difference between CAC and CACB is negligible. Although the summation

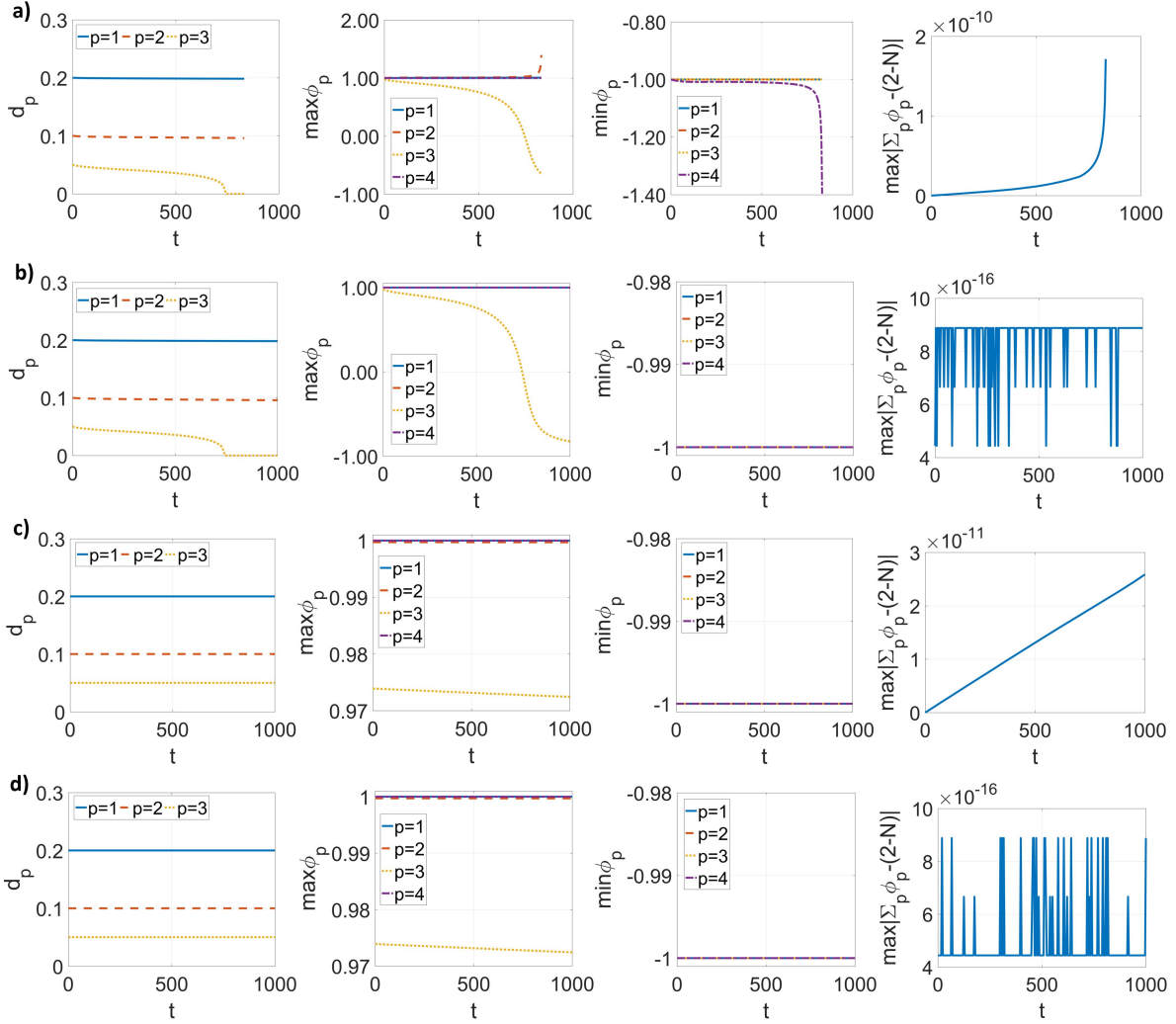


Figure 2: Results of the under-resolved structures from a) CH, b) CHB, c) CAC, and d) CACB. The first column: Diameter of the circles. The second column: Maximum of the order parameters. The third column: Minimum of the order parameters. The fourth column: Error of the summation constraint for the order parameters.

constraint for the order parameters is satisfied, as shown in Fig.2, it is enforced more accurately when the boundedness mapping is included.

In summary, CAC has a better ability to preserve under-resolved structures than CH. The boundedness mapping is beneficial to improve the robustness of the scheme and to provide a physical solution.

4.3 Large-Density-Ratio advection

An appropriate coupling between the Phase-Field models and the momentum equation Eq.(19) should satisfy the consistencies of mass conservation and of mass and momentum transport. The large-density-ratio advection is performed to demonstrate that the consistency conditions are achieved at the discrete level.

The domain considered is $[1 \times 1]$ and its boundaries are all periodic. $[128 \times 128]$ cells are used to discretize the domain and the time step is $\Delta t = 0.1h$. Neither the viscosity of the fluids nor the surface force is considered. The densities of Phases 1, 2, and 3 are 10^6 , 10^3 , and 1, respectively. We set $\eta = 3h$, $M_0 = 10^{-7}$, and the off-diagonal elements of $\lambda_{p,q}$ are $\frac{0.03}{2\sqrt{2}}\eta$. Phase 1 is enclosed by a circle at $(0.65, 0.65)$ with a radius 0.15. Phase 2 is enclosed by a circle at $(0.3, 0.4)$ with a radius 0.1. Phase 3 occupies the rest

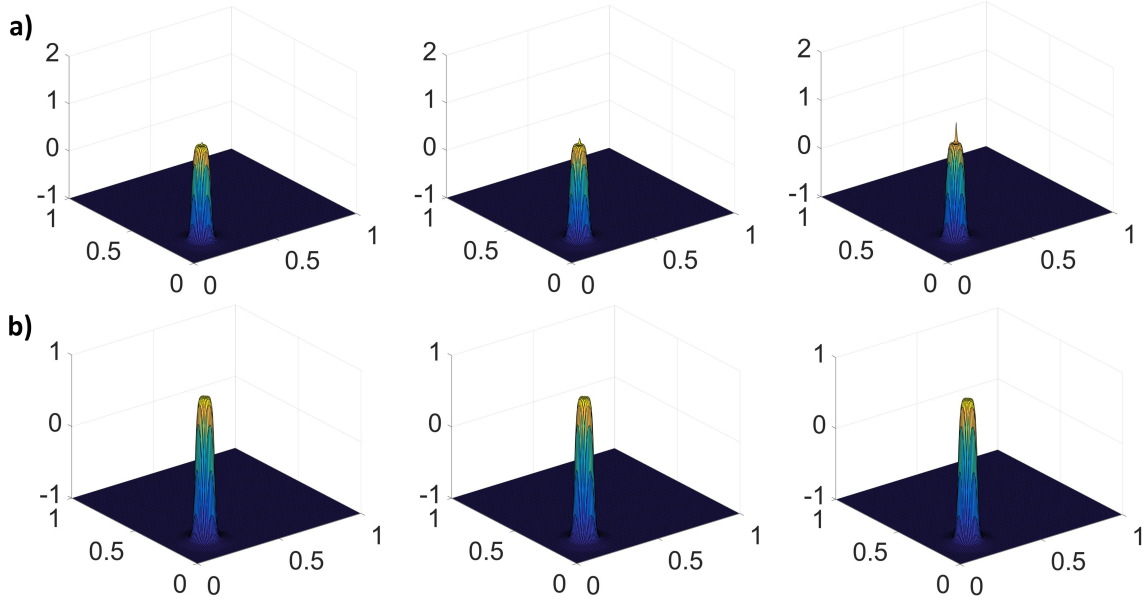


Figure 3: Profiles of ϕ_2 at selected moments of the under-resolved structures from a) CH and b) CHB. The first column: $t = 781.2500$. The second column: $t = 820.3125$. The third column: $t = 832.0313$.

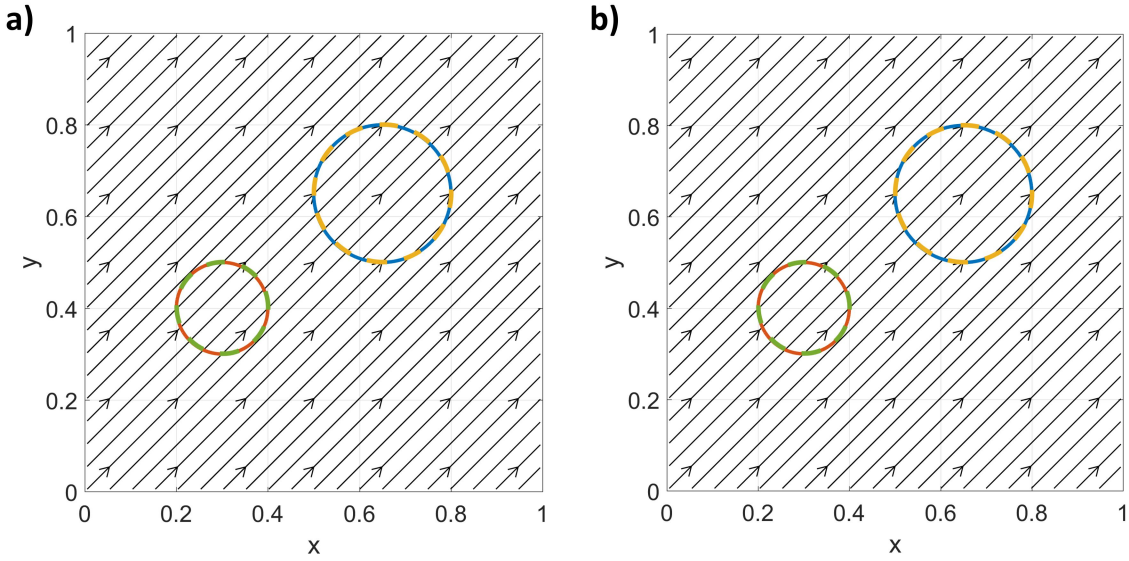


Figure 4: Results of the large-density-ratio advection from a) CHB and b) CACB. Blue solid line: Interface of phase 1 at $t = 0$. Red solid line: Interface of phase 2 at $t = 0$. Yellow dashed line: Interface of phase 1 at $t = 1$. Green dashed line: Interface of phase 2 at $t = 1$. Black arrow: Stream lines at $t = 1$.

of the domain. Initially, the velocity is homogeneous, i.e., $u|_{t=0} = v|_{t=0} = 1$.

The interfaces should be translated by the homogeneous velocity, without any deformation. At the same time, the translation of the interfaces should not change the velocity. These should be true, independent of the density ratio. Therefore, at $t = 1$, the interfaces should return to their original locations. Fig.4 shows the results from CHB and CACB. At $t = 1$, the interfaces return to their original locations without any deformation and the velocity preserves its initial value, even though the maximum density ratio is 10^6 .

The critical factor in the problem is to satisfy the consistency of mass conservation and the consistency of mass and momentum transport. Thanks to the consistent formulation Eq.(28), Eq.(33) is satisfied and, as

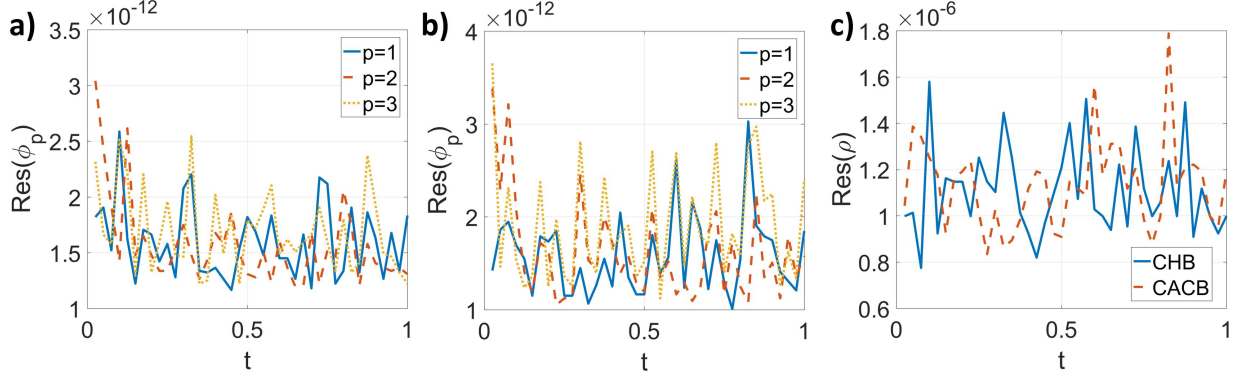


Figure 5: Residues of Eq.(33) and Eq.(35) of the large-density-ratio advection from CHB and CACB. a) Residue of Eq.(33) from CHB. b) Residue of Eq.(33) from CACB. c) Residue of Eq.(35) from CHB and CACB.

a result, the discrete mass conservation equation Eq.(35) is satisfied as well by using the discrete mass flux Eq.(34) which is applied in the momentum equation. Fig.5 shows the residues of Eq.(33) and Eq.(35) from CHB and CACB. The residue of Eq.(33) from either CHB or CACB is on the order of the round-off error. The residue of Eq.(35) is on the order of the maximum density ratio of the problem times the residue of Eq.(33). Violating these consistency conditions can introduce unphysical velocity fluctuations and interface deformation, which trigger the instability in large-density-ratio problems. This has been demonstrated in previous studies, e.g., [29, 27, 28].

4.4 Horizontal shear layer

To demonstrate the properties of the Phase-Field models when they are coupled to the flow dynamics, the three-phase horizontal shear layer is performed. The domain considered is $[1 \times 1]$ and its boundaries are all periodic. The domain is discretized by $[128 \times 128]$ cells and the time step is $\Delta t = 0.1h$. The density of phase 1 is 50 and its viscosity is 0.01. Phase 2 has a density 10 and a viscosity 0.1. The density and viscosity of phase 3 are 1 and 0.05, respectively. The surface tensions are $\sigma_{1,2} = 0.05$, $\sigma_{1,3} = 0.01$, and $\sigma_{2,3} = 0.1$. We set $\eta = h$ and $M_0 = 10^{-7}$. Initially, phase 1 is at $y_0 < y < y_2$ and is stationary. Phase 2 is at $y_1 < y < y_0$ and is moving to the right with a unity speed. Phase 3 is at the rest of the domain and is moving to the left with a unity speed. We set $y_0 = 0.5$, $y_1 = 0.25$, and $y_2 = 0.75$. A sinusoidal vertical velocity is added, whose amplitude is 0.05 and wavelength is 2π .

We first investigate the mass conservation of individual phases Eq.(3), the maximum and minimum of the order parameters, and the summation constraint for the order parameters Eq.(1). The results from CH, CHB, CAC, and CACB are shown in Fig.6. It is clear that all the results satisfy the mass conservation and the summation constraint for the order parameters, no matter whether the boundedness mapping is included. However, without the boundedness mapping, i.e., from CH and CAC, the order parameters do not stay in the physical interval $[-1, 1]$. The out-of-bound error appears at about $t = 0.4$. It grows with time and finally reaches $O(10^{-4})$. On the other hand, with the help of the boundedness mapping, none of the order parameters go beyond the physical interval $[-1, 1]$.

Next, we quantify the problem by the time histories of the kinetic energy,

$$E_K = \int_{\Omega} \frac{1}{2} \rho (u^2 + v^2) d\Omega,$$

the free energy,

$$E_F = \int_{\Omega} \sum_{p,q=1}^N \frac{\lambda_{p,q}}{2} \left(\frac{1}{\eta^2} (g_1(\phi_p) + g_1(\phi_q) - g_2(\phi_p + \phi_q)) - \nabla \phi_p \cdot \nabla \phi_q \right) d\Omega,$$

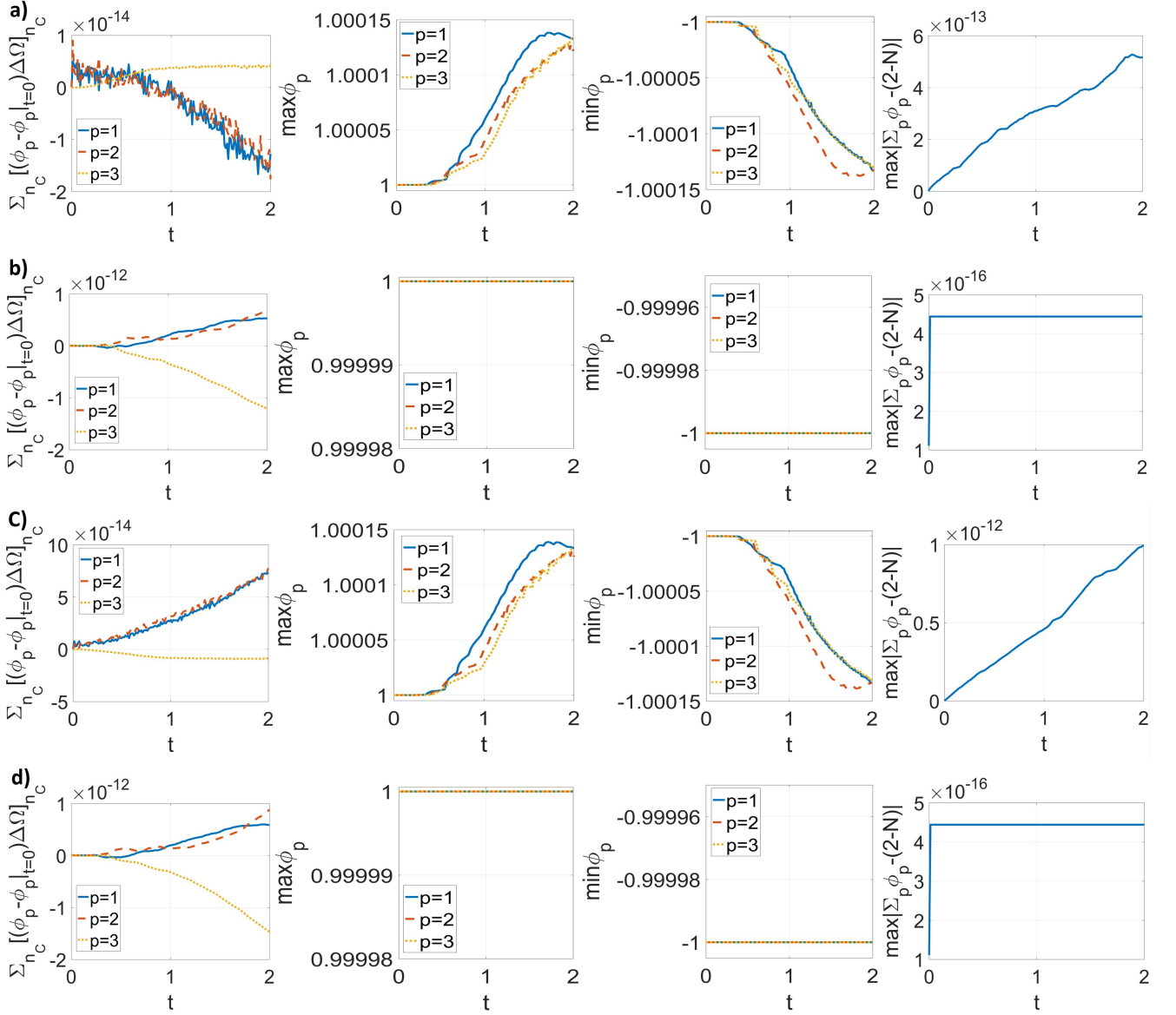


Figure 6: Results of the three-phase horizontal shear layer from a) CH, b) CHB, c) CAC, and d) CACB. The first column: Errors of the mass conservation of individual phases. The second column: Maximum of the order parameters. The third column: Minimum of the order parameters. The fourth column: Error of the summation constraint for the order parameters.

and the total energy,

$$E_T = E_K + \frac{1}{2}E_F,$$

and they are shown in Fig.7. The results with/without the boundedness mapping are on top of each other since the out-of-bound error is small. In addition, the difference between CHB and CACB is unobservable in this case. The decay of the total energy is consistent with the energy law in [27].

We finally validate the consistency of reduction by adding the 4th phase, whose density is 0.5, viscosity is 0.08, and surface tensions are $\sigma_{1,4} = 0.08$, $\sigma_{2,4} = 0.02$, and $\sigma_{3,4} = 0.2$. However, Phase 4 is absent at the beginning, i.e., $\phi_4|_{t=0} = -1$. Therefore, it should not appear during computation. The results from CHB and CACB are shown in Fig.8. The mass conservation and the summation constraint for the order parameters

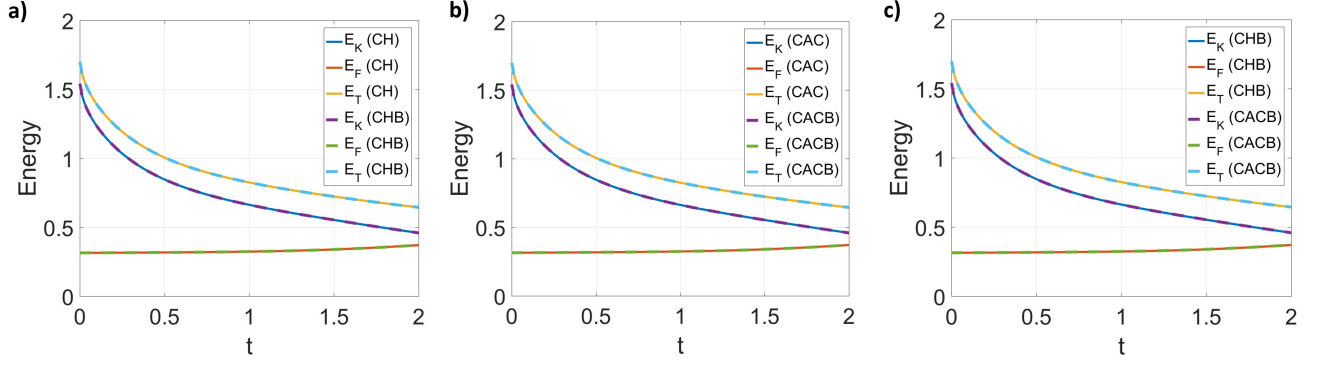


Figure 7: Time histories of the energies from a) CH and CHB, b) CAC and CACB, and c) CHB and CACB.

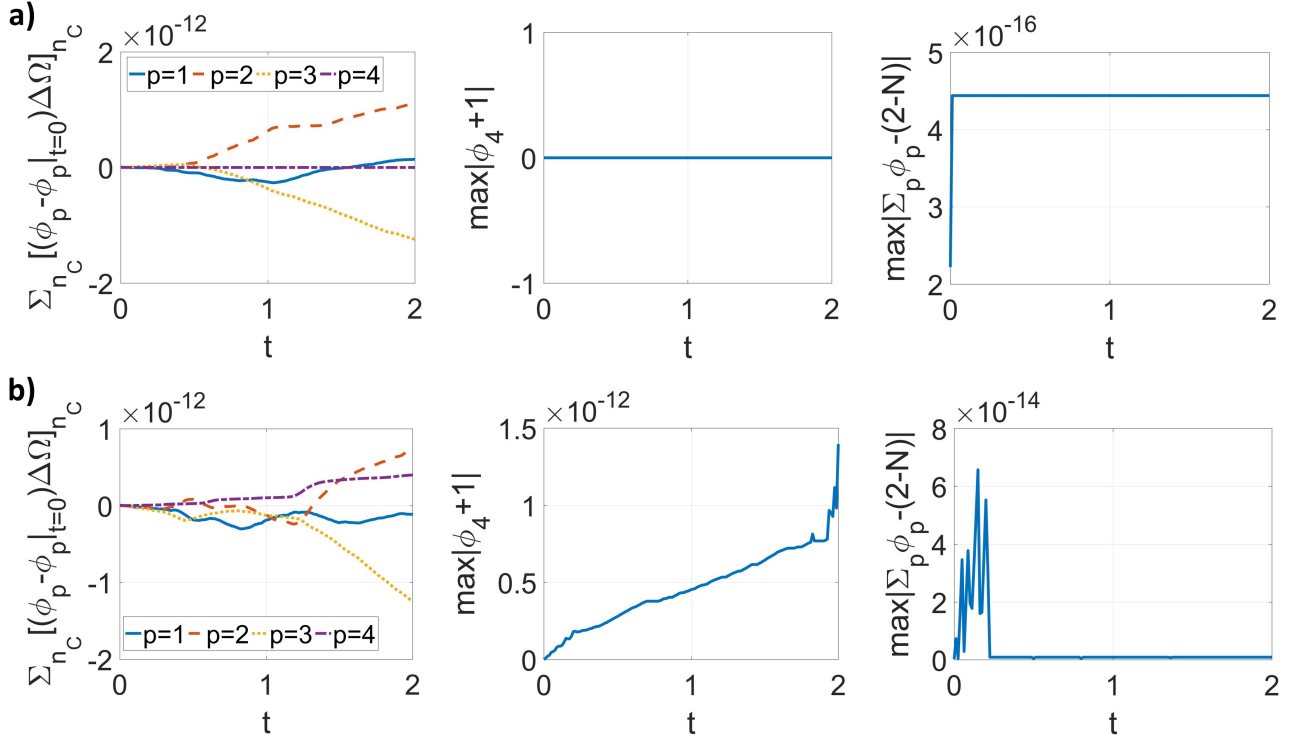


Figure 8: Results of the four-phase horizontal shear layer from a) CHB and b) CACB. The first column: Errors of the mass conservation of individual phases. The second column: Error of ϕ_4 . The third column: Error of the summation constraint for the order parameters.

are again satisfied. ϕ_4 from CHB is exact -1 at every cell and every time step. However, the difference between ϕ_4 from CACB and -1 is the round-off error. Therefore, both the Phase-Field models along with the boundedness mapping do not generate any fictitious phases. Then we compare the energies from the three-phase case to those from the 4-phase case in Fig.9, and the difference between them is unobservable. The three-phase dynamics is reproduced by the four-phase set up with a phase absent. Therefore the consistency of reduction is satisfied.

In summary, with the proposed schemes, the order parameters satisfy their summation constraint, the mass conservation, and the consistency of reduction. They, in addition, are bounded in their physical interval if the boundedness mapping is supplemented.

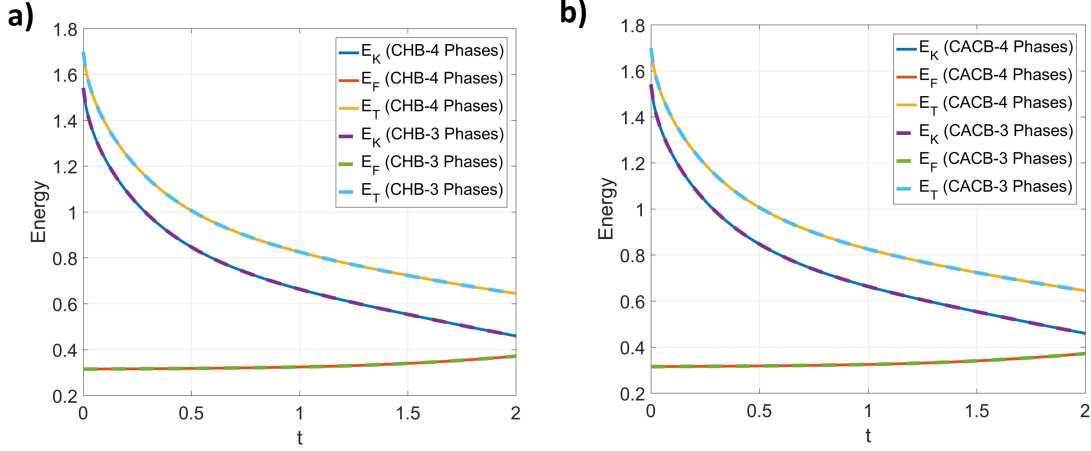


Figure 9: Time histories of the energies from a) CHB and b) CACB.

4.5 Convergence tests

The convergence behaviors of the models and schemes are investigated. In the first test, we fix η and M_0 in order to study the convergence of the numerical solutions to the exact solutions of the Phase-Field models. This test is related to the truncation error and should be able to indicate the formal order of accuracy of the schemes. In the second test, η and M_0 are correlated to the grid/cell size h . The interface thickness η is reduced when the cell is refined, and the convergence of the numerical solutions of the Phase-Field models to the sharp-interface solution can be studied.

The domain considered is $[1 \times 2]$ with free-slip boundaries at the left and right, and with no-slip boundaries at the top and bottom. The number of cells on a unite length is ranging from 16 to 256, and the time step is proportional to the cell size, i.e., $\Delta t = 0.128h$. The density and viscosity of phase 1 are 1 and 0.1, while the density and viscosity of phase 2 are 1000 and 10. The surface tension is 1.96, and the gravity is 0.98 pointing downward. Initially, the flow is stationary and a circular bubble of phase 1 is at $(0.5, 0.5)$ with a radius 0.25. The computation is stopped at $t = 1$. The same set up is considered in [30], and the sharp-interface solution is available and well-validated in the time period considered. The circularity

$$\psi_c = \frac{P_a}{P_b} = \frac{2\sqrt{\int_{\phi_1 > 0} \pi d\Omega}}{P_b},$$

where P_b and P_a are the perimeters of the rising bubble and of the circle whose area is identical to the bubble, the center of mass

$$y_c = \frac{\int_{\Omega} y \frac{1+\phi_1}{2} d\Omega}{\int_{\Omega} \frac{1+\phi_1}{2} d\Omega},$$

and the rising velocity

$$v_c = \frac{\int_{\Omega} v \frac{1+\phi_1}{2} d\Omega}{\int_{\Omega} \frac{1+\phi_1}{2} d\Omega},$$

are defined as the benchmark quantities of the problem.

Fig.10 and Fig.11 show the results from CHB and CACB, respectively, using fixed $\eta = \eta_0 = \frac{1}{32}$ and $M_0 = 10^{-7}$. As the cell size becomes smaller, the numerical solutions gradually approach the exact solutions of the Phase-Field models, which is different from the sharp-interface solution, since the interface thickness is not reducing. To quantify the convergence behavior, we compute the L_2 errors, i.e., the root-mean-square errors, of the three benchmark quantities. We consider the solutions from the finest grid as the exact solutions of the Phase-Field models. The errors are summarized in Table 1, and the convergence rates are 2nd-order. Therefore, the schemes for CHB and CACB are formally 2nd-order accurate.

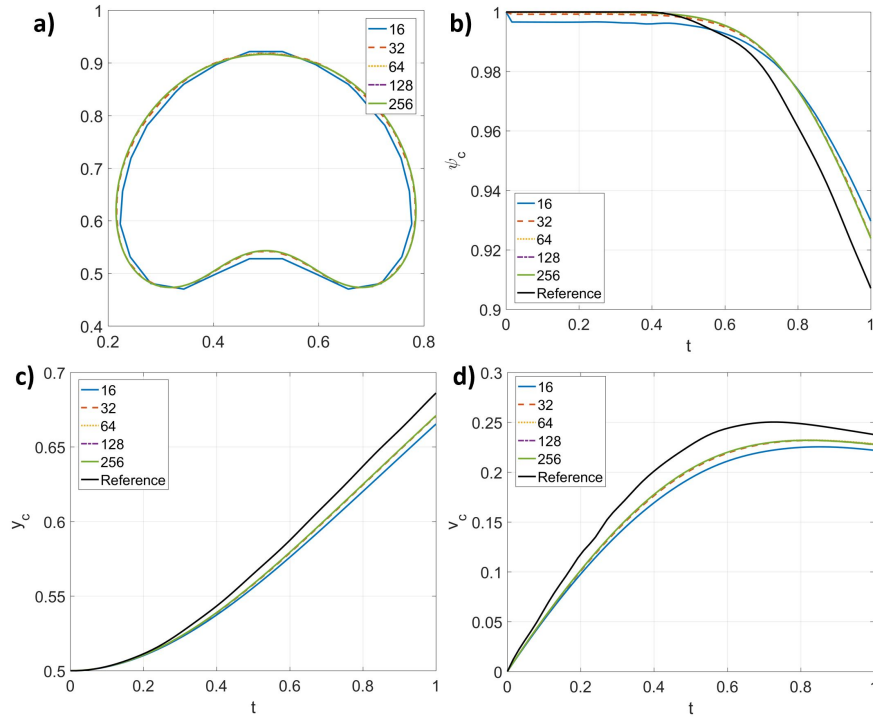


Figure 10: Results of the convergence test with $\eta = \eta_0$ from CHB. a) Shape of the bubble at $t = 1$. b) Circularity. c) Center of mass. d) Rising velocity. 16, 32, 64, 128, and 256 are the numbers of cells on a unite length of the domain. Reference is the sharp-interface solution.

Table 1: L_2 errors of the convergence test with $\eta = \eta_0$

Grid	CHB						CACB					
	ψ_c		γ_c		v_c		ψ_c		γ_c		v_c	
	L_2	order	L_2	order	L_2	order	L_2	order	L_2	order	L_2	order
16	3.09e-3	2.36	3.199e-3	3.26	6.76e-3	3.07	3.09e-3	2.35	3.18e-3	3.30	6.71e-3	3.07
32	6.03e-4	2.06	3.34e-4	2.50	8.06e-4	1.80	6.05e-4	1.99	3.23e-4	2.45	7.96e-4	1.39
64	1.45e-4	2.53	5.90e-5	2.23	2.31e-4	2.53	1.52e-4	2.582	5.91e-5	2.31	3.05e-4	2.18
128	2.51e-5		1.26e-5		3.99e-5		2.54e-5		1.19e-5		6.74e-5	

Fig.12 and Fig.13 show the results from CHB and CACB, respectively, using $\eta = h$ and $M_0 = 10^{-7}(\eta/\eta_0)$. The convergence of the numerical solutions from the Phase-Field models to the sharp-interface solution is observed, as the cell size, as well as the interface thickness, is refined. The L_2 errors of the three benchmark quantities are computed using the sharp-interface solution. The errors are summarized in Table 2, and both CHB and CACB share a similar convergence behavior. The circularity ψ_c , which quantifies the shape of the bubble, converges to the sharp-interface solution at a rate close to 2nd-order. The convergence rate is around 1.5th-order for the dynamics of the bubble, quantified by both γ_c and v_c . Therefore, the numerical solutions of the Phase-Field models converge to the sharp-interface solution.

The same studies have been performed in [27] for CH and a similar convergence behavior is observed. Therefore, the boundedness mapping has little effect on either the formal order of accuracy or the convergence rate to the sharp-interface solution.

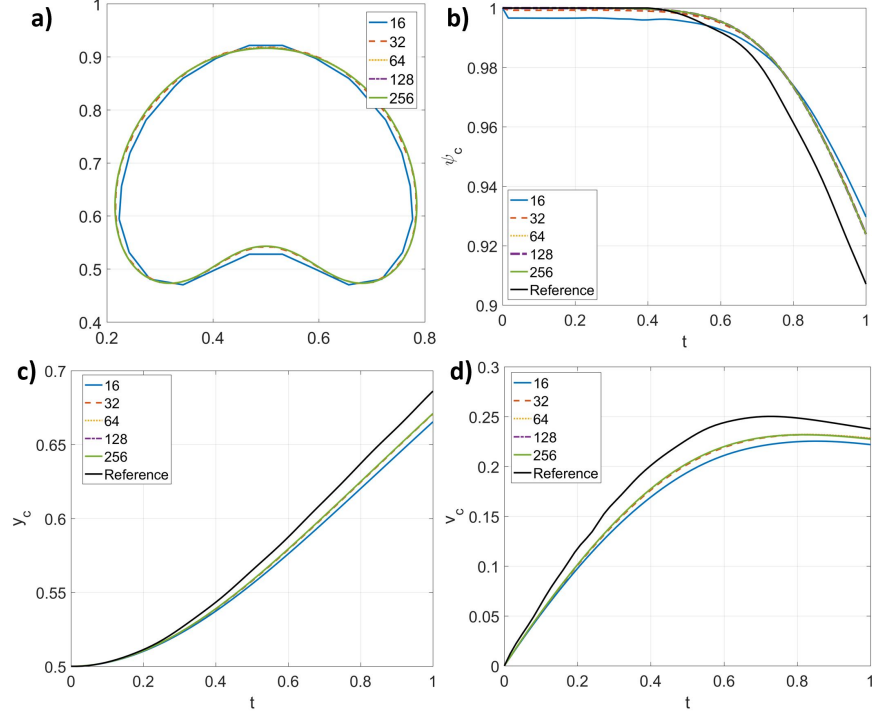


Figure 11: Results of the convergence test with $\eta = \eta_0$ from CACB. a) Shape of the bubble at $t = 1$. b) Circularity. c) Center of mass. d) Rising velocity. 16, 32, 64, 128, and 256 are the numbers of cells on a unite length of the domain. Reference is the sharp-interface solution.

Table 2: L_2 errors of the convergence test with $\eta = h$

Grid	CHB						CACB					
	ψ_c		y_c		v_c		ψ_c		y_c		v_c	
	L_2	order	L_2	order	L_2	order	L_2	order	L_2	order	L_2	order
16	1.93e-2	1.34	2.83e-2	1.64	5.62e-2	1.55	1.93e-2	1.33	2.84e-2	1.64	5.62e-2	1.55
32	7.64e-3	1.97	9.09e-3	1.82	1.92e-2	1.52	7.65e-3	1.97	9.09e-3	1.82	1.92e-2	1.52
64	1.96e-3	1.72	2.58e-3	1.61	6.67e-3	1.11	1.95e-3	1.78	2.58e-3	1.62	6.66e-3	1.12
128	5.96e-4		8.46e-4		3.09e-3		5.69e-4		8.39e-4		3.06e-3	

4.6 Three-Phase dam break

To demonstrate the capability of the proposed CHB and CACB models for complicated multiphase problems, the three-phase dam-break problem is performed.

The three phases considered are water (phase 1), whose density is 998.207kg/m^3 and viscosity is $1.002 \times 10^{-3}\text{Pa} \cdot \text{s}$, oil (phase 2), whose density is 557kg/m^3 and viscosity is $9.15 \times 10^{-2}\text{Pa} \cdot \text{s}$, and air (phase 3), whose density is 1.2041kg/m^3 and viscosity is $1.78 \times 10^{-5} \times 10^{-2}\text{Pa} \cdot \text{s}$. The surface tensions between them are $\sigma_{1,2} = 0.04\text{N/m}$, $\sigma_{1,3} = 0.0728\text{N/m}$, and $\sigma_{2,3} = 0.055\text{N/m}$. The gravity is pointing downward with a magnitude 9.8m/s^2 . The governing equations are non-dimensionalized by a density scale 1.204kg/m^3 , a length scale 5.715cm , and an acceleration scale 9.8m/s^2 . The domain considered is $[8 \times 2]$ and all the boundaries are no-slip. The domain is discretized by $[512 \times 128]$ cells. η and M_0 are 0.01 and 10^{-7} , respectively. The time step is $\Delta t = 5 \times 10^{-4}$. Initially, the flow is stationary, a square water column with a

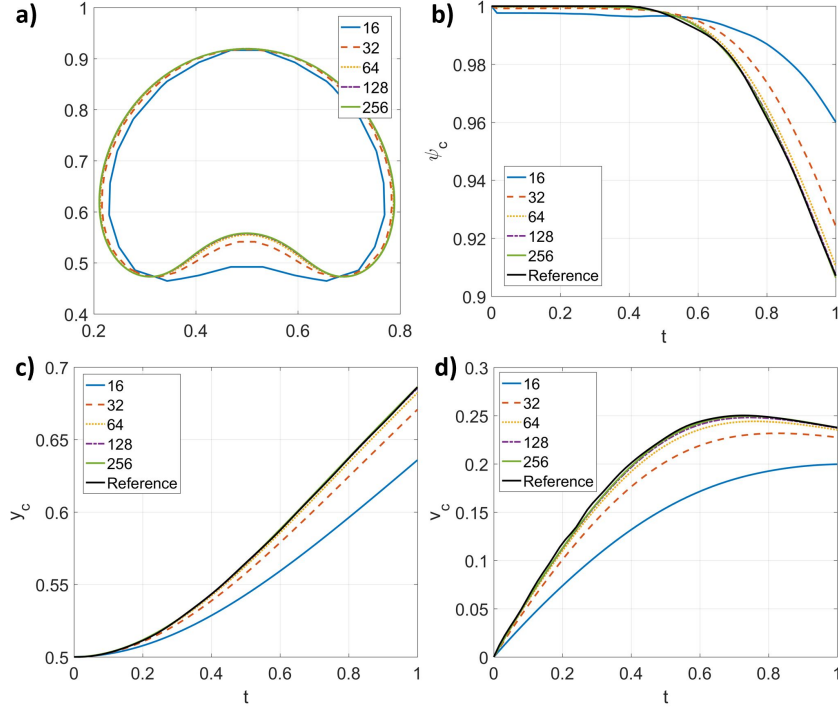


Figure 12: Results of the convergence test with $\eta = h$ from CHB. a) Shape of the bubble at $t = 1$. b) Circularity. c) Center of mass. d) Rising velocity. 16, 32, 64, 128, and 256 are the numbers of cells on a unite length of the domain. Reference is the sharp-interface solution.

width 1 is at the left of the domain, and an oil column with the same size is at the right of the domain.

The initial dynamics is quantified by measuring the front Z and height H of the water column. Since the water and oil are far away separated at the beginning, there is no interaction between them and we can compare the numerical solutions from both CHB and CACB to the experimental data from Martin and Moyce [48]. We calibrate the numerical results by setting Z equal to 1.44, when t is 0.8, and H equal to 1, when t is 0, as those in [48]. The results are shown in Fig.14. The difference between CHB and CACB is unobservable and both results agree well with the experimental data.

Fig.15 and Fig.16 show the configurations of the interfaces from CHB and CACB, respectively, up to $t = 10$. Both models give a similar picture of the problem. The water and oil columns collapse at the beginning and start sliding along the bottom wall. The water is moving faster than the oil since the oil is about 100 times more viscous than the water. Due to the high viscosity, the oil close to the lateral wall is falling down more slowly than other parts of it. When the fronts of the water and oil meet together, the oil, which is lighter and moving slower, is squeezed upward by the water, and the water climbs along the bottom of the oil. The front of the oil, squeezed by the water, collapses again and lays above the water, along with breaking up into small droplets and filaments. At the same time, the water keeps moving toward the right and pushing the oil at the bottom moving backward. It can be observed that the interactions among different phases are very complicated. Even though the problem is challenging, the mass conservation and the summation constraint for the order parameters are always satisfied, as shown in Fig.17.

Fig.18 shows the results from CHC, which is CH but including the clipping and rescaling steps in the boundedness mapping. The results are compared to those from CHB. Thanks to adding the rescaling step, the summation constraint for the order parameters are satisfied. The mass change due to simply clipping and rescaling the order parameters is significant, although the out-of-bound error is small, on the order of 10^{-5} , in one time step. The problem is sensitive to out-of-bound errors since it has a maximum density ratio of about 1000 and a maximum viscosity ratio of about 5000. Both the clipping operation in previous studies and the boundedness mapping proposed in the present work improve the robustness of the scheme, which is important for the success of the simulation. However, the boundedness mapping additionally enforces the

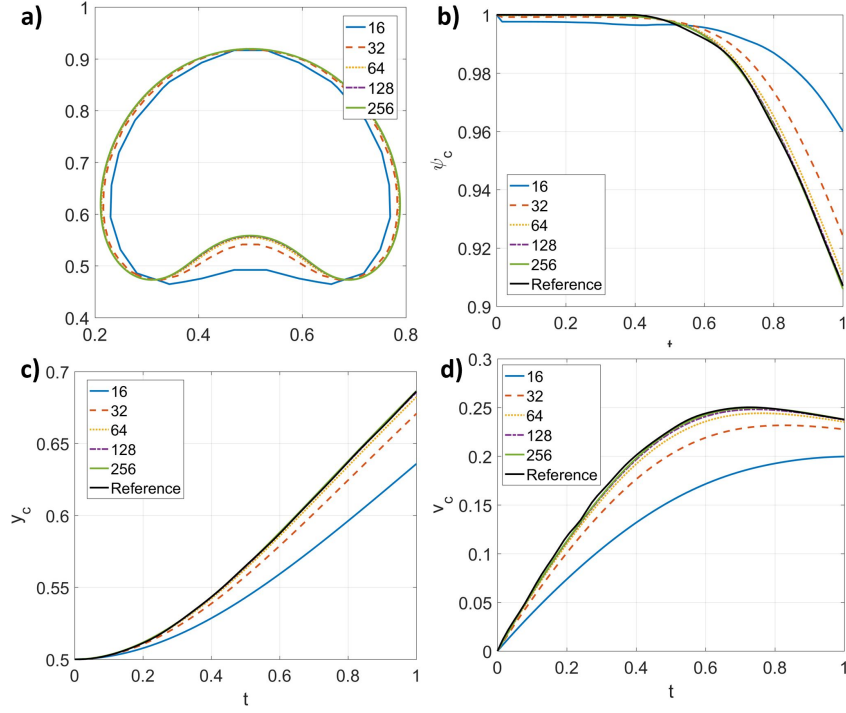


Figure 13: Results of the convergence test with $\eta = h$ from CACB. a) Shape of the bubble at $t = 1$. b) Circularity. c) Center of mass. d) Rising velocity. 16, 32, 64, 128, and 256 are the numbers of cells on a unite length of the domain. Reference is the sharp-interface solution.

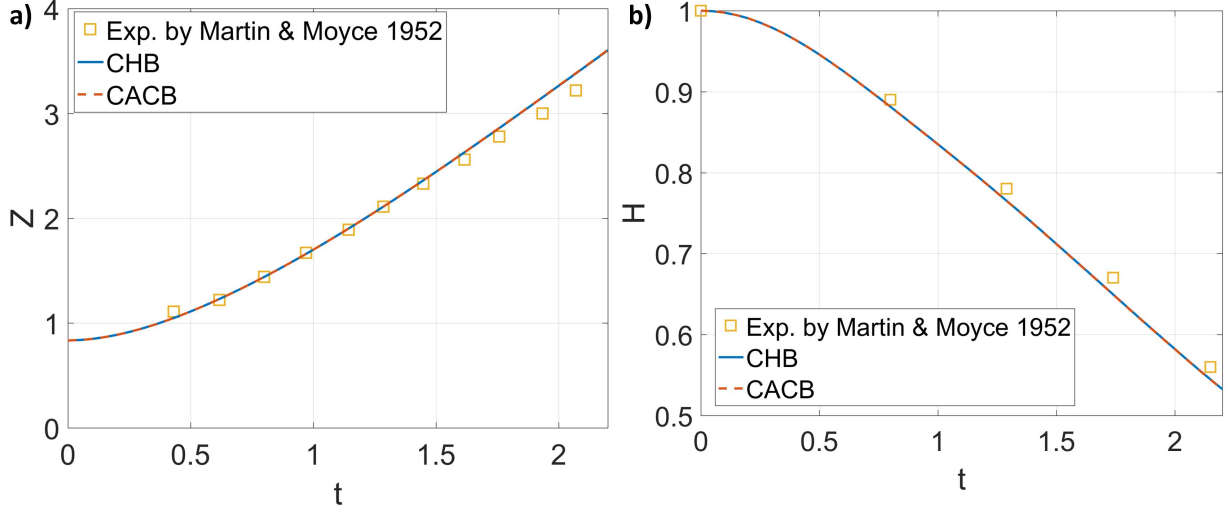


Figure 14: Front and height of the water column vs. t . a) Front of the water column. b) Height of the water column.

mass conservation of each phase, which is also important for long-time simulation.

5 Conclusion

In the present work, the general multiphase volume distribution problem is addressed consistently and conservatively by the proposed algorithm. The algorithm honors the summation constraint, conservation

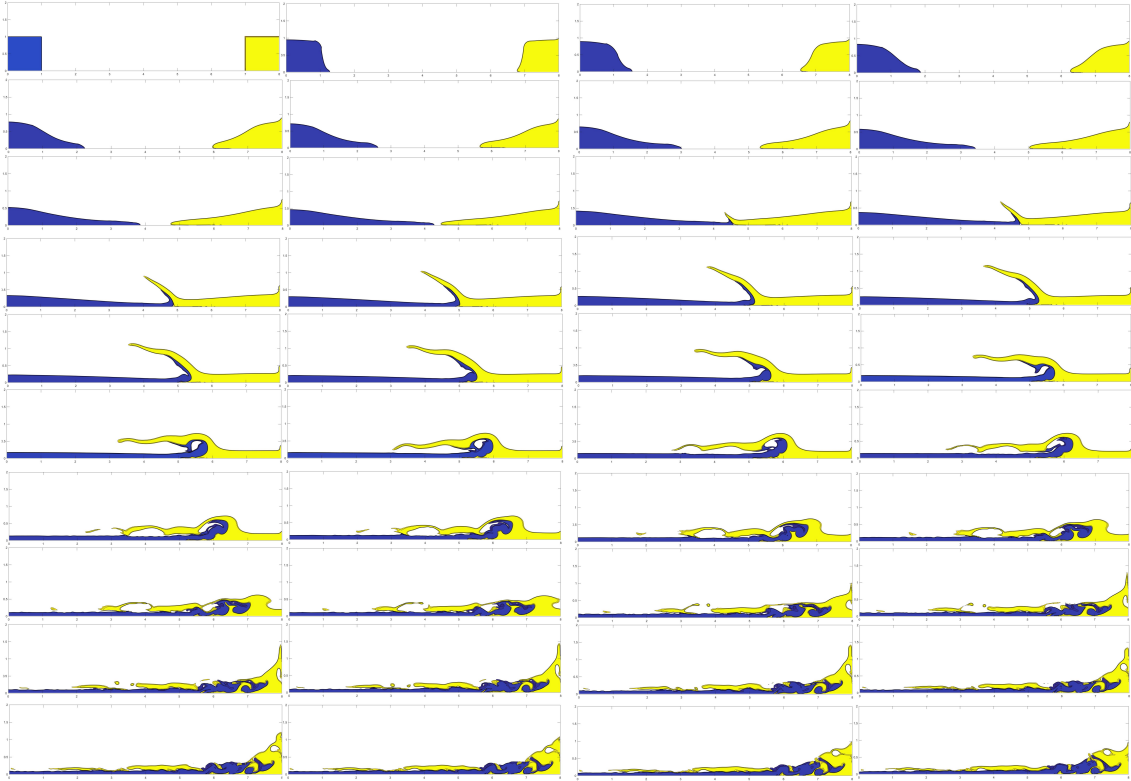


Figure 15: Configurations of the three-phase dam break from CHB at $t = 0.00, 0.50, 0.75, 1.00, \dots, 10.00$. Blue: Water (phase 1). Yellow: Oil (phase 2). White: Air (phase 3).

constraint, and consistency of reduction, so that no fictitious phases, voids, or overfilling are generated after the volume distribution. It is challenging to satisfy all the constraints for a general multiphase case, and we discover that the phase-wise formula, which works for two-phase problems, is not feasible. Then the problem is turned into a linear system representing the interactions among different phases. A weight function for volume distribution is carefully selected, so that the aforementioned constraints are satisfied and the coefficient matrix of the linear system is not only symmetric but also diagonally dominant. A scaling argument is supplemented so that the solution of the linear system is admissible. To the best of our knowledge, this is the first volume distribution algorithm that is general for an arbitrary number of phases and satisfies all the physical constraints mentioned.

The first application of the proposed volume distribution algorithm is to develop a multiphase conservative Allen-Cahn model that honors the summation constraint for the order parameters, the mass conservation, and the consistency of reduction, simultaneously. To the best of our knowledge, such a reduction-consistent multiphase conservative Allen-Cahn model has not been reported in previous studies. In addition, the multiphase Allen-Cahn model exactly reduces to the one proposed in [7] for two-phase problems. A corresponding numerical scheme is developed for the multiphase conservative Allen-Cahn model, and we show that the scheme preserves the physical properties of the model at the discrete level. The consistency of reduction is an important property of a multiphase model and its scheme, since it eliminates any generation of fictitious phases. Our numerical studies show that fictitious phases are unphysically generated at interfacial regions by a multiphase model that violates the consistency of reduction. On the other hand, there are no fictitious phases generated by either the multiphase conservative Allen-Cahn model, proposed in the present work, or the multiphase Cahn-Hilliard model, studied in our previous work [27], since both the models and their schemes are reduction consistent. A comparison study is also performed and it shows that the conservative Allen-Cahn model has a better ability than the Cahn-Hilliard model to preserve the under-resolved structures.

The second application of the proposed volume distribution algorithm is to develop the boundedness

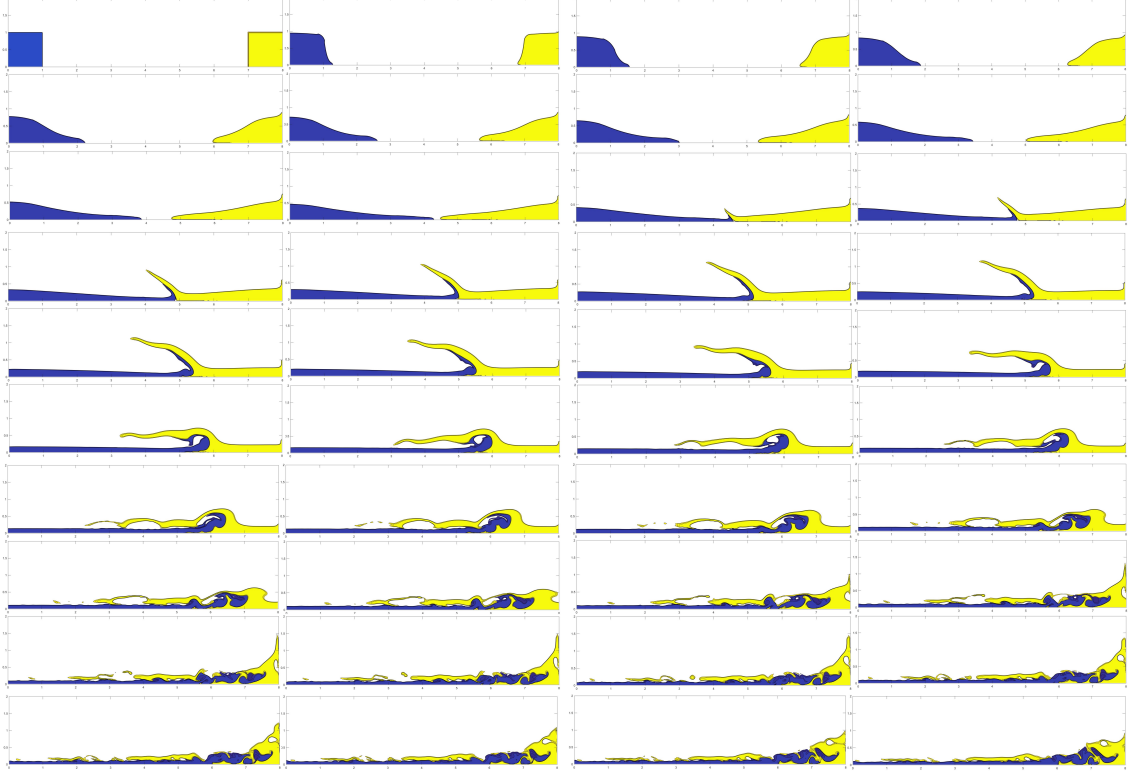


Figure 16: Configurations of the three-phase dam break from CACB at $t = 0.00, 0.50, 0.75, 1.00, \dots, 10.00$. Blue: Water (phase 1). Yellow: Oil (phase 2). White: Air (phase 3).

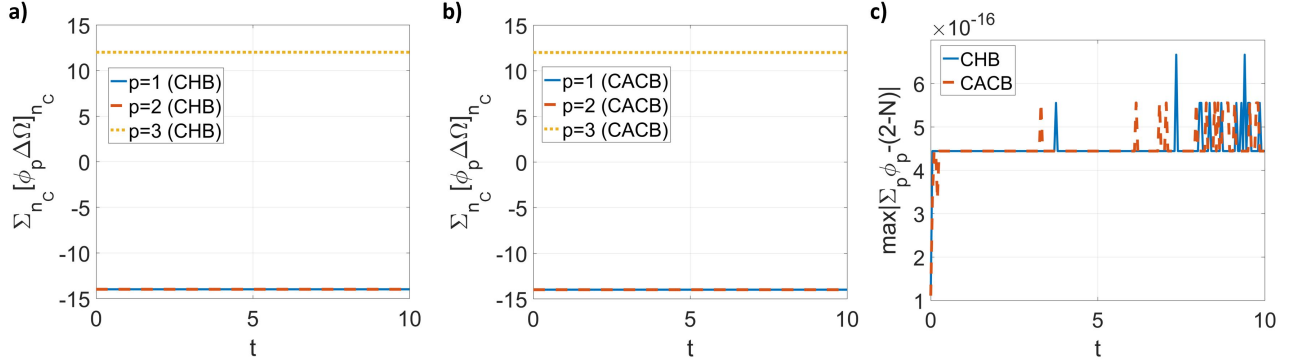


Figure 17: Results of the three-phase dam break. a) Mass conservation of individual phases from CHB. b) Mass conservation of individual phases from CACB. c) Error of the summation constraint for the order parameters from CHB and CACB.

mapping, which is a numerical procedure to address the out-of-bound order parameters resulting from either the defect of a multiphase model or the numerical error. The out-of-bound order parameters can lead to a negative density or viscosity, especially when the density or viscosity ratio of a problem is large. The boundedness mapping maps the out-of-bound order parameters into their physical interval but does not violate the physical properties of the order parameters, i.e., their summation constraint, mass conservation, and consistency of reduction. The boundedness mapping is applied to both the multiphase Cahn-Hilliard and conservative Allen-Cahn models. Along with the proposed consistent and conservative schemes for those models, the order parameters are consistent, conservative, and bounded, which has been carefully analyzed and numerically validated. It is observed in the numerical tests that the out-of-bound error can grow as

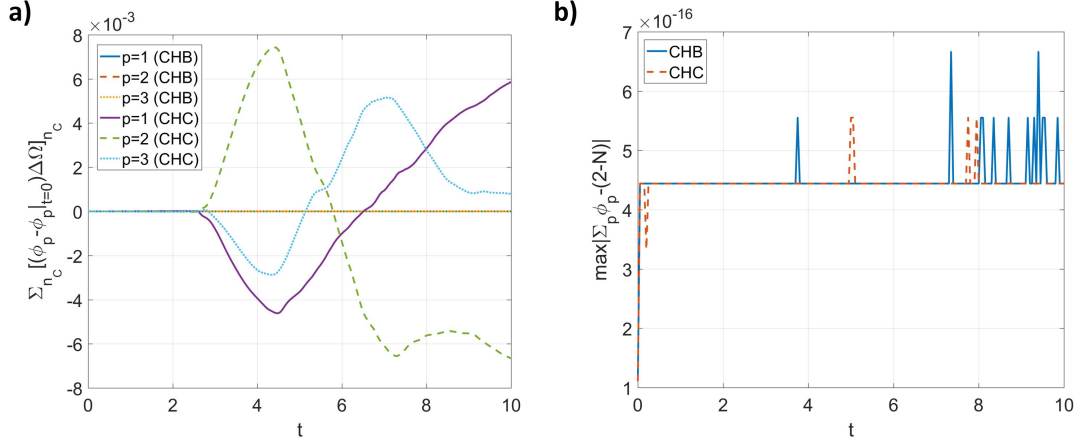


Figure 18: Results of the three-phase dam break from CHB and CHC (which is CH but including the clipping and rescaling steps in the boundedness mapping). a) Errors of mass conservation of individual phases. b) The Error of the summation constraint for the order parameters.

the computation goes on, contaminate the physical solution, and in the end, trigger numerical instability, although it is small in one time step. The boundedness mapping removes the out-of-bound error while preserves the physical properties of the order parameters, which is beneficial to improve the robustness of the scheme and to provide a physical solution.

The multiphase Phase-Field models are coupled with the momentum equation to model multiphase flows. Thanks to the consistent formulation proposed in our previous work [28], in addition to the consistency of reduction, the consistency of mass conservation and the consistency of mass and momentum transport are satisfied, which is numerically demonstrated by successfully performing an advection problem having a density ratio 10^6 . The overall scheme for multiphase flows, including the scheme for the multiphase Cahn-Hilliard model in our previous work [27] or the scheme for the multiphase conservative Allen-Cahn model in the present work, the boundedness mapping, the consistent formulation [28], and the scheme for the momentum equation [29, 27], is shown to satisfy the mass conservation of each phase, the momentum conservation without interfacial tensions, the summation constraint for the order parameters, the boundedness of the order parameters, and the consistency conditions. The momentum including interfacial tensions can be conserved by the conservative method for the surface force, see [27]. The convergence tests show that the proposed schemes are formally 2nd-order accurate, and that the numerical Phase-Field solutions from both the Cahn-Hilliard and conservative Allen-Cahn models converge to the sharp-interface solution with similar behavior. In addition, the boundedness mapping does not influence either the order of accuracy of the scheme or the convergence behavior to the sharp-interface solution. A complicated three-phase dam-break problem, which has large density and viscosity ratios, is performed to demonstrate the capability of the Phase-Field models in multiphase flows. The numerical solutions agree well with the experimental data, and strong interactions among different phases are captured. The mass conservation and the summation constraint for the order parameters are always satisfied even though the problem considered is highly dynamical. The results also show that simply clipping and rescaling the order parameters, instead of performing the boundedness mapping, leads to significant mass changes.

In summary, the multiphase volume distribution problem is appropriately addressed in the present work and two applications of it are performed. The first one is at the continuous level, developing the multiphase conservative Allen-Cahn model that satisfies the consistency of reduction. The second one is at the discrete level, developing the boundedness mapping that maps the out-of-bound order parameters into their physical interval. Therefore, the consistent and conservative volume distribution algorithm is an important tool for modeling and simulating multiphase flows.

Acknowledgments

A.M. Ardekani would like to acknowledge the financial support from the National Science Foundation (CBET-1705371). This work used the Extreme Science and Engineering Discovery Environment (XSEDE) [71], which is supported by the National Science Foundation grant number ACI-1548562 through allocation TG-CTS180066 and TG-CTS190041. G. Lin would like to acknowledge the support from National Science Foundation (DMS-1555072 and DMS-1736364, CMMI-1634832 and CMMI-1560834), and Brookhaven National Laboratory Subcontract 382247.

References

- [1] H. Abels, H. Garcke, and G. Grun. Thermodynamically consistent, frame indifferent diffuse interface models for incompressible two-phase flows with different densities. *Mathematical Models and Methods in Applied Sciences*, 22:1150013, 2012.
- [2] D.M. Anderson, G.B. McFadden, and A.A. Wheeler. Diffuse-interface methods in fluid mechanics. *Annu. Rev. Fluid Mech.*, 30:139–165, 1998.
- [3] A. Baraldi, M.S. Dodd, and A. Ferrante. A mass-conserving volume-of-fluid method: Volume tracking and droplet surface-tension in incompressible isotropic turbulence. *Comput. Fluids*, 96:322–337, 2014.
- [4] F. Boyer, C. Lapuerta, S. Minjeaud, B. Piar, and M. Quintard. Cahn-hilliard/navier-stokes model for the simulation of three-phase flows. *Transport in Porous Media*, 82(3):463–483, 2010.
- [5] F. Boyer and S. Minjeaud. Hierarchy of consistent n-component cahn–hilliard systems. *Math. Models Methods Appl. Sci.*, 24:2885–292, 2014.
- [6] J.U. Brackbill, D.B. Kothe, and C. Zemach. A continuum method for modeling surface tension. *J. Comput. Phys.*, 100:335–354, 1992.
- [7] M. Brassel and E. Bretin. A modified phase field approximation for mean curvature flow with conservation of the volume. *Math Method Appl. Sci.*, 10:1157–1180, 2011.
- [8] M. Bussmann, D.B. Kothe, and J.M. Sicilian. Modeling high density ratio incompressible interfacial flows. In *Proceedings of ADME Fluid Engineering Division Summer Meeting*, page 31125, 2002.
- [9] W. Chen, C. Wang, X. Wang, and S.M. Wise. Positivity-preserving, energy stable numerical schemes for the cahn-hilliard equation with logarithmic potential. *J. Comput. Phys. X*, 3:100031, 2019.
- [10] V.L. Chenadec and H. Pitsch. A monotonicity preserving conservative sharp interface flow solver for high density ratio two-phase flows. *J. Comput. Phys.*, 249:185–203, 2013.
- [11] R. Chiodi and O. Desjardins. A reformulation of the conservative level set reinitialization equation for accurate and robust simulation of complex multiphase flows. *J. Comput. Phys.*, 343:186–200, 2017.
- [12] P-H Chiu and Y-T Lin. A conservative phase-field method for solving incompressible two-phase flows. *J. Comput. Phys.*, 230:185–204, 2011.
- [13] S. Dong. An efficient algorithm for incompressible n-phase flows. *J. Comput. Phys.*, 276:691–728, 2014.
- [14] S. Dong. Physical formulation and numerical algorithm for simulating n immiscible incompressible fluids involving general order parameters. *J. Comput. Phys.*, 836:98–128, 2015.
- [15] S. Dong. Wall-bounded multiphase flows of nimmiscible incompressible fluids: Consistency and contact-angle boundary condition. *J. Comput. Phys.*, 338:21–67, 2017.
- [16] S. Dong. Multiphase flows of n immiscible incompressible fluids: A reduction-consistent and thermodynamically-consistent formulation and associated algorithm. *J. Comput. Phys.*, 361:1–49, 2018.

- [17] S. Dong and J. Shen. A time-stepping scheme involving constant coefficient matrices for phase-field simulations of two-phase incompressible flows with large density ratios. *J. Comput. Phys.*, 231:5788–5804, 2012.
- [18] R.P. Fedkiw, T. Aslam, B. Merriman, and S. Osher. A non-oscillatory eulerian approach to interfaces in multimaterial flows (the ghost fluid method). *J. Comput. Phys.*, 152:457–492, 1999.
- [19] M.M. Francois. Recent numerical and algorithmic advances within the volume tracking framework for modeling interfacial flows. *Procedia IUTAM*, 15:270–277, 2015.
- [20] M.M. Francois, J.S. Cummins, E.D. Dendy, D.B. Kothe, M.J. Sicilian, and W.W. Williams. A balanced-force algorithm for continuous and sharp interfacial surface tension models within a volume tracking framework. *J. Comput. Phys.*, 213:141–173, 2006.
- [21] F. Frank, A. Rupp, and D. Kuzmin. Bound-preserving flux limiting schemes for dg discretizations of conservation laws with applications to the cahn-hilliard equation. *Comput. Methods Appl. Mech. Engrg.*, 359:112665, 2020.
- [22] D. Fuster, T. Arrufat, M. Cialesi-Esposito, Y. Ling, L. Malan, S. Pal, R. Scardovelli, G. Tryggvason, and S. Zaleski. A momentum-conserving, consistent, volume-of-fluid method for incompressible flow on staggered grids. *arXiv:1811.12327 [physics.comp-ph]*, 2018.
- [23] F. Gibou, R. Fedkiw, and S. Osher. A review of level-set methods and some recent applications. *J. Comput. Phys.*, 353:82–109, 2018.
- [24] D. Gueyffier, J. Li, A. Nadim, R. Scardovelli, and S. Zaleski. Volume-of-fluid interface tracking with smoothed surface stress methods for three-dimensional flows. *J. Comput. Phys.*, 152:423–456, 1999.
- [25] C.W. Hirt and B.D. Nichols. Volume of fluid (vof) method for the dynamics of free boundaries. *J. Comput. Phys.*, 39:201–225, 1981.
- [26] Z. Huang, G. Lin, and A.M. Ardekani. A mixed upwind/central weno scheme for incompressible two-phase flows. *J. Comput. Phys.*, 387:455–480, 2019.
- [27] Z. Huang, G. Lin, and A.M. Ardekani. A consistent and conservative phase-field method for multiphase incompressible flows. *arXiv:2010.01099 [physics.comp-ph]*, 2020.
- [28] Z. Huang, G. Lin, and A.M. Ardekani. Consistent and conservative scheme for incompressible two-phase flows using the conservative allen-cahn model. *J. Comput. Phys.*, 420:109718, 2020.
- [29] Z. Huang, G. Lin, and A.M. Ardekani. Consistent, essentially conservative and balanced-force phase-field method to model incompressible two-phase flows. *J. Comput. Phys.*, 406:109192, 2020.
- [30] S. Hysing, S. Turek, D. Kuzmin, N. Parolini, E. Burman, S. Ganesan, and L. Tobiska. Quantitative benchmark computations of two-dimensional bubble dynamics. *Int. J. Numer. Methods. Fluids*, 60:1259–1288, 2009.
- [31] Satoshi Ii, Kazuyasu Sugiyama, Shintaro Takeuchi, Shu Takagi, Yoichiro Matsumoto, and Feng Xiao. An interface capturing method with a continuous function: The thinc method with multi-dimensional reconstruction. *J. Comput. Phys.*, 231(5):2328–2358, 2012.
- [32] D. Jacqmin. Calculation of two-phase navier-stokes flows using phase-field modeling. *J. Comput. Phys.*, 155:96–127, 1999.
- [33] D. Jeong and J. Kim. Conservative allen-cahn-navier-stokes system for incompressible two-phase fluid flows. *Comput. Fluids*, 156:239–246, 2017.
- [34] G-S Jiang and C-W Shu. Efficient implementation of weighted eno schemes. *J. Comput. Phys.*, 126:202–228, 1996.

- [35] V. Joshi and R.K. Jaiman. An adaptive variational procedure for the conservative and positivity preserving allen-cahn phase-field model. *J. Comput. Phys.*, 336:478–504, 2018.
- [36] V. Joshi and R.K. Jaiman. A positivity preserving and conservative variational scheme for phase-field modeling of two-phase flows. *J. Comput. Phys.*, 360:137–166, 2018.
- [37] J. Kim. Phase field computations for ternary fluid flows. *Comput. Methods Appl. Mech. Engre.*, 196:4779–4788, 2007.
- [38] J. Kim. A generalized continuous surface tension force formulation for phase-field models for multi-component immiscible fluid flows. *Comput. Methods Appl. Mech. Engre.*, 198:3105–3112, 2009.
- [39] J. Kim. Phase-field models for multi-component fluid flows. *Commun. Comput. Phys.*, 12:613–661, 2012.
- [40] J. Kim and H.G. Lee. A new conservative vector-valued allen-cahn equation and its fast numerical method. *Comput. Phys. Commun.*, 221:102–108, 2017.
- [41] J. Kim, S. Lee, and Y. Choi. A conservative allen-cahn equation with a space-time dependent lagrange multiplier. *Int. J. Eng. Sci.*, 84:11–17, 2014.
- [42] J. Kim and J. Lowengrub. Phase field modeling and simulation of three-phase flows. *Interfaces Free Bound.*, 7:435–466, 2005.
- [43] B. Lallane, L.R. Villegas, S. Tanguy, and F. Risso. On the computation of viscous terms for incompressible two-phase flows with level set/ghost fluid method. *J. Comput. Phys.*, 301:289–307, 2015.
- [44] D. Lee and J. Kim. Comparison study of the conservative allen-cahn and the cahn-hilliard equations. *Math. Comput. Simulation*, 119:35–56, 2016.
- [45] H.G. Lee and J. Kim. An efficient numerical method for simulating multiphase flows using a diffuse interface model. *Physica A*, 423:33–50, 2015.
- [46] F. Losasso, T. Shinar, A. Selle, and R. Fedkiw. Multiple interacting liquids. *ACM Transactions on Graphics (TOG)*, 25(3):812–819, 2006.
- [47] F. Magaletti, F. Picano, M. Chinappi, L. Marino, and C.M. Casciola. The sharp-interface limit of the cahn-hilliard/navier-stokes model for binary fluids. *J. Fluid Mech.*, 714:95–126, 2013.
- [48] J.C. Martin and W.J. Moyce. An experimental study of the collapse of liquid columns on a rigid horizontal plane. *Philosophical Transactions of the Royal Society of London, Series A*, 244:312–324, 1952.
- [49] S. Mirjalili, C.B. Ivey, and A. Mani. A conservative diffuse interface method for two-phase flows with provable boundedness properties. *J. Comput. Phys.*, 401:109006, 2020.
- [50] S. Mirjalili, S. Jain, and Dodd M.S. Interface-capturing methods for two-phase flos: An overview and recent developments. *Center for Turbulence Research Annual Research Briefs*, pages 117–135, 2017.
- [51] Abu-Al-Saud M.O., S. Popinet, and H.A. Tchelepi. A conservative and well-balanced surface tension model. *J. Comput. Phys.*, 371:896–931, 2018.
- [52] N. Nangia, E.G. Boyce, N.A. Patankar, and A.P.S. Bhalla. A robust incompressible navier-stokes solver for high density ratio multiphase flows. *J. Comput. Phys.*, 390:548–594, 2019.
- [53] E. Olsson and G. Kreiss. A conservative level set method for two phase flow. *J. Comput. Phys.*, 210:225–246, 2005.
- [54] E. Olsson, G. Kreiss, and S. Zahedi. A conservative level set method for two phase flow ii. *J. Comput. Phys.*, 225:785–807, 2007.

- [55] S. Osher and A.J. Sethian. Fronts propagating with curvature-dependent speed: Algorithms based on hamilton-jacobi formulations. *J. Comput. Phys.*, 79:12–49, 1988.
- [56] M. Owkes and O. Desjardins. A mass and momentum conserving unsplit semi-lagrangian framework for simulating multiphase flows. *J. Comput. Phys.*, 332:21–46, 2017.
- [57] S. Popinet. Numerical models for surface tension. *Annu. Rev. Fluid Mech.*, 50:49–75, 2018.
- [58] A. Prosperetti and G. Tryggvason. *Computational Methods for Multiphase Flow*. Cambridge University Press, 2007.
- [59] L. Qian, Y. Wei, and F. Xiao. Coupled thinc and level set method: A conservative interface capturing scheme with high-order surface representations. *J. Comput. Phys.*, 373:284–303, 2018.
- [60] M. Raessi and H. Pitsch. Consistent mass and momentum transport for simulating incompressible interfacial flows with large density ratios using the level set method. *Comput. Fluids*, 63:70–81, 2012.
- [61] Abadi R.H.H., M.H. Rahimian, and A. Fakhari. Conservative phase-field lattice-boltzmann model for ternary fluids. *J. Comput. Phys.*, 374:668–691, 2018.
- [62] M. Rudman. A volume-tracking method for incompressible multifluid flows with large density variations. *Int. J. Numer. Methods. Fluids*, 28:357–378, 1998.
- [63] R. Scardovelli and S. Zaleski. Direct numerical simulation of free-surface and interfacial flow. *Annu. Rev. Fluid Mech.*, 31:567–603, 1999.
- [64] S.P. Schofield, R.V. Garimella, M.M. Francois, and R. Loubere. A second-order accurate material-order-independent interface reconstruction technique for multi-material flow simulations. *J. Comput. Phys.*, 228:731–745, 2009.
- [65] S.P. Schofield, Christon M.A., V. Dyadechko, R.V. Garimella, R.B. Lowrie, and B.K. Swartz. Multi-material incompressible flow simulation using the moment-of-fluid method. *Int. J. Numer. Meth. Fluids*, 63:931–952, 2010.
- [66] J.A. Sethian and P. Smereka. Level set method for fluid interfaces. *Annu. Rev. Fluid Mech.*, 35:341–372, 2003.
- [67] J. Shen. Modeling and numerical approximation of two-phase incompressible flows by a phase-field approach. *Multiscale Modeling and Analysis for Materials Simulation*, 22:147–195, 2011.
- [68] D.P. Starinshak, S. Karni, and P.L. Roe. A new level set model for multimaterial flows. *Interface and free boundaries*, 4:263–276, 2002.
- [69] M. Sussman, P. Smereka, and S. Osher. A level set approach for computing solutions to incompressible two-phase flow. *J. Comput. Phys.*, 114:146–159, 1994.
- [70] G. Tierra and F. Guillen-Gonzalez. Numerical methods for solving the cahn-hilliard equation and its applicability to related energy-based models. *Arch Computat Methods Eng*, 22:269–289, 2015.
- [71] J. Towns, T. Cockerill, M. Dahan, I. Foster, K. Gaither, A. Grimshaw, V. Hazlewood, S. Lathrop, D. Lifka, G.D. Peterson, R. Roskies, J.R. Scott, and N. Wilkins-Diehr. Xsede: accelerating scientific discovery. *Comput. Sci. Eng.*, 16:62–74, 2014.
- [72] G. Tryggvason, B. Bunner, A. Esmaeeli, D. Juric, N. Al-Rawahi, W. Tauber, J. Han, S. Nas, and Y.J. Jan. A front-tracking method for the computations of multiphase flow. *J. Comput. Phys.*, 169:708–759, 2001.
- [73] G. Tryggvason, R. Scardovelli, and S. Zaleski. *Direct Numerical Simulations of Gas-Liquid Multiphase Flows*. Cambridge University Press, 2011.

- [74] S.O. Unverdi and G. Tryggvason. A front-tracking method for viscous, incompressible, multi-fluid flows. *J. Comput. Phys.*, 100:25–37, 1992.
- [75] F Xiao, Y Honma, and T Kono. A simple algebraic interface capturing scheme using hyperbolic tangent function. *Int. J. Numer. Meth. Fluids*, 48(9):1023–1040, 2005.
- [76] B. Xie, Jin P., Du. Y., and S. Liao. A consistent and balanced-force model for incompressible multiphase flows on polyhedral unstructured grids. *International Journal of Multiphase Flow*, 122:103125, 2020.
- [77] B. Xie and F. Xiao. Toward efficient and accurate interface capturing on arbitrary hybrid unstructured grids: The thinc method with quadratic surface representation and gaussian quadrature. *J. Comput. Phys.*, 349:415–440, 2017.
- [78] Z. Yang and S. Dong. Multiphase flows of nimmiscible incompressible fluids: Anoutflow/open boundary condition and algorithm. *J. Comput. Phys.*, 366:33–70, 2018.
- [79] P. Yue, J.J. Feng, C. Liu, and J. Shen. A diffuse-interface method for simulating two-phase flows of complex fluids. *J. Fluid Mech.*, 515:293–317, 2004.
- [80] P. Yue, C. Zhou, and J.J. Feng. Spontaneous shrinkage of drops and mass conservation in phase-field simulations. *J. Comput. Phys.*, 223:1–9, 2007.
- [81] C.Y. Zhang, H. Ding, P. Gao, and Y.L. Wu. Diffuse interface simulation of ternary fluids in contact with solid. *J. Comput. Phys.*, 309:37–51, 2016.
- [82] Q. Zhang and X.P. Wang. Phase field modeling and simulation of three-phase flow on solid surfaces. *J. Comput. Phys.*, 319:79–107, 2016.
- [83] T. Zhang, J. Wu, and X. Lin. An interface-compressed diffuse interface method and its application for multiphase flows. *Physics of Fluids*, 31:122102, 2019.